Cell

Ligand binding initiates single-molecule integrin conformational activation

Graphical abstract

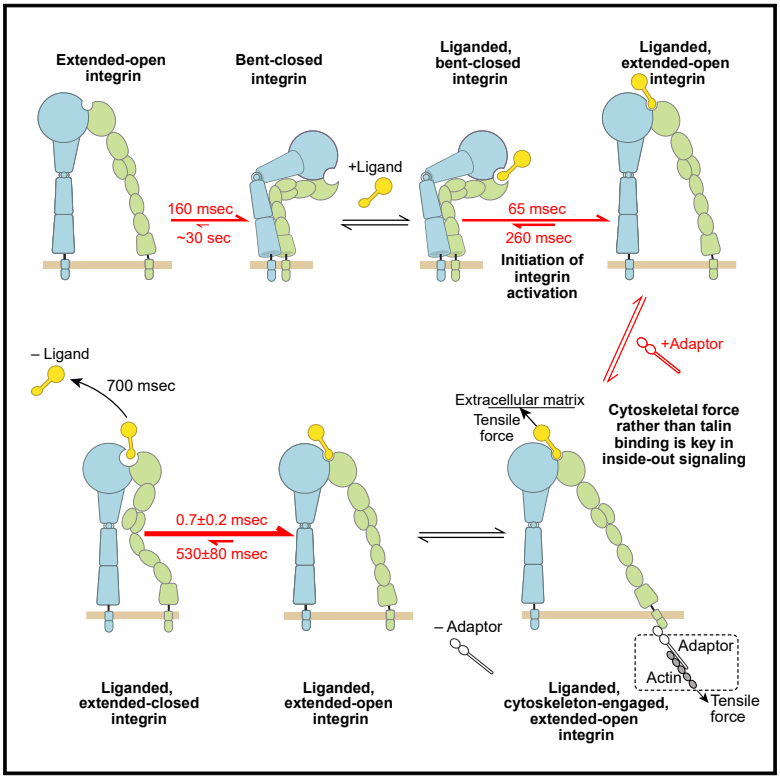

Highlights

- Conformational transitions in unliganded, intact integrins take ~30 s
- 65 ms after ligand binding, integrins transit to the high-affinity state
- Integrin leg extension and headpiece opening are concerted, not independent
- Talin modestly stabilizes but does not induce integrin extension or opening

Authors

Jing Li, Myung Hyun Jo, Jiabin Yan, ..., Sophia Yan, Taekjip Ha, Timothy A. Springer

Correspondence

taekjip.ha@childrens.harvard.edu (T.H.), springer@crystal.harvard.edu (T.A.S.)

In brief

Viewing integrins in action through single molecules shows that ligand-dependent activation is the predominant factor initiating signaling.

Li et al., 2024, Cell *187*, 2990–3005
June 6, 2024
https://doi.org/10.1016/j.cell.2024.04.049

CellPress

CellPress
OPEN ACCESS

Cell

Article

Ligand binding initiates single-molecule integrin conformational activation

Jing Li,[1,2,3,6] Myung Hyun Jo,[1,2,6] Jiabin Yan,[1,3] Taylor Hall,[1,3] Joon Lee,[1,3] Uriel López-Sánchez,[1,3] Sophia Yan,[1,4] Taekjip Ha,[1,2,5,7,*] and Timothy A. Springer[1,3,7,8,*]

[1]Program in Cellular and Molecular Medicine, Boston Children's Hospital, Boston, MA 02115, USA
[2]Department of Pediatrics, Harvard Medical School, Boston, MA 02115, USA
[3]Department of Biological Chemistry and Molecular Pharmacology, Harvard Medical School, Boston, MA 02115, USA
[4]Newton South High School, Newton, MA 02459, USA
[5]Howard Hughes Medical Institute, Boston, MA 02115, USA
[6]These authors contributed equally
[7]These authors contributed equally
[8]Lead contact
*Correspondence: taekjip.ha@childrens.harvard.edu (T.H.), springer@crystal.harvard.edu (T.A.S.)
https://doi.org/10.1016/j.cell.2024.04.049

SUMMARY

Integrins link the extracellular environment to the actin cytoskeleton in cell migration and adhesiveness. Rapid coordination between events outside and inside the cell is essential. Single-molecule fluorescence dynamics show that ligand binding to the bent-closed integrin conformation, which predominates on cell surfaces, is followed within milliseconds by two concerted changes, leg extension and headpiece opening, to give the high-affinity integrin conformation. The extended-closed integrin conformation is not an intermediate but can be directly accessed from the extended-open conformation and provides a pathway for ligand dissociation. In contrast to ligand, talin, which links the integrin β-subunit cytoplasmic domain to the actin cytoskeleton, modestly stabilizes but does not induce extension or opening. Integrin activation is thus initiated by outside-in signaling and followed by inside-out signaling. Our results further imply that talin binding is insufficient for inside-out integrin activation and that tensile force transmission through the ligand-integrin-talin-actin cytoskeleton complex is required.

INTRODUCTION

> Soul, 1: The immaterial essence, animating principle...
>
> www.Merriam-Webster.com

Integrins link ligands embedded in the extracellular environment to the cytoskeleton to provide the traction for cell migration and adhesion and regulate cell differentiation and growth.[1] Yet despite the wide importance of integrins in development, homeostasis, disease, and therapeutics, the mechanism of integrin activation is incompletely understood. Integrins must undergo large-scale conformational change between the bent-closed low-affinity state to the high-affinity extended-open conformation to stably bind ligand[2–4] (Figure 1A). Of the 24 integrin heterodimers, 22 bind the cytoskeletal adaptor talin to their β-subunit cytoplasmic domains to connect to the actin cytoskeleton and transmit tensile force to their ligands to carry out cellular functions.[5–9] The talin head domain, which can bind to integrin cytoplasmic domains but not to the actin cytoskeleton, and thus cannot function physiologically, has nonetheless been reported to be sufficient to activate integrins. A common view in the integrin field is that activation is initiated from inside the cell, with talin binding hypothesized to be the key initiating event.[6,10–13]

The term integrin inside-out signaling was coined when it was discovered that integrins on resting T lymphocytes did not adhere to ligands on substrates unless the T cell receptor for antigen or intracellular kinases were activated.[15] However, when cells in suspension were similarly stimulated, only small increases in affinity were observed that required multimeric ligand or sensitive assays for detection, consistent with the importance of force transmission between the actin cytoskeleton and ligand-bound substrate in stabilizing integrins in their active states. The dominant integrin conformational changes detected with antibodies occur not with activation of cells in suspension, but after integrins have bound ligand on substrates.[16] When cells adhere through integrins to ligands on substrates, the actin cytoskeleton exerts pN range forces on ligands[6] and integrin cytoplasmic domains[17]; integrins also align in the direction of actin flow.[18] While G-protein coupled receptors and receptor tyrosine kinases stimulate integrin adhesiveness on platelets and leukocytes, it is now clear that actin polymerization is stimulated at the same time.[19] Thus, the key step in integrin inside-out activation might be force

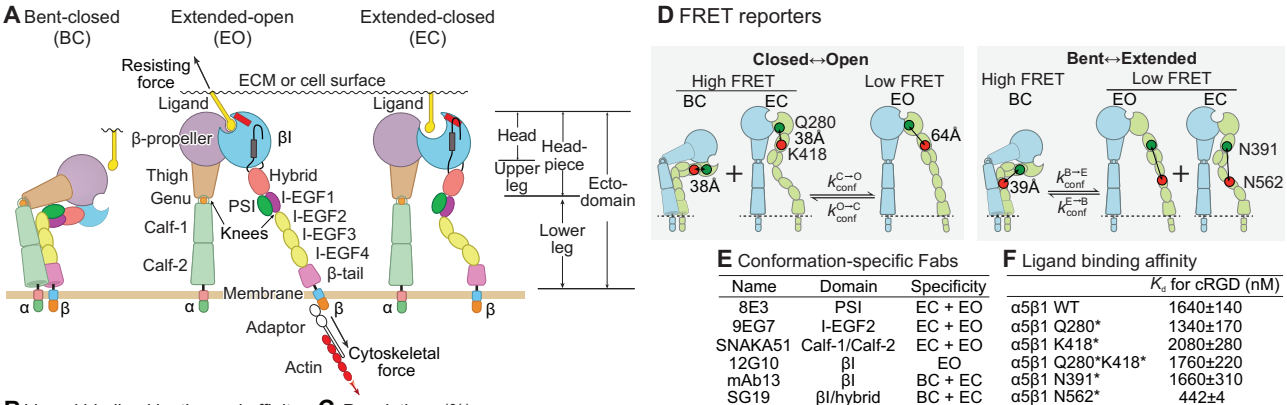

B Ligand binding kinetics and affinity

	k_{on} (10^4 $M^{-1}s^{-1}$)	k_{off} (10^{-3} s^{-1})	K_d (nM)
BC	35±6	1400±400	4000±2100
EC	35±6	1400±400	4000±2100
EO	7.5±0.3	0.082±0.021	1.4±0.1

C Populations (%)

	Ectodomain		Full-length on cell surface		Full-length in LMNG/CHS	
	– lig	+ lig	– lig	+ lig	– lig	+ lig
BC	52.2	0.05	99.82	15.9	98.7±0.4	6.0±3.8
EC	17.1	0.03	0.01	0.002	0.8±0.3	0.05±0.04
EO	30.7	99.9	0.17	84.1	0.5±0.2	93.8±3.8

E Conformation-specific Fabs

Name	Domain	Specificity
8E3	PSI	EC + EO
9EG7	I-EGF2	EC + EO
SNAKA51	Calf-1/Calf-2	EC + EO
12G10	βI	EO
mAb13	βI	BC + EC
SG19	βI/hybrid	BC + EC

F Ligand binding affinity

	K_d for cRGD (nM)
α5β1 WT	1640±140
α5β1 Q280*	1340±170
α5β1 K418*	2080±280
α5β1 Q280*K418*	1760±220
α5β1 N391*	1660±310
α5β1 N562*	442±4
α5β1 N391*N562*	1120±110

Figure 1. Integrin conformational states and their FRET reporters

(A) Overall integrin conformational states.

(B) Intrinsic ligand binding kinetics and affinity of each state in integrin α5β1.[3,4,14]

(C) Populations of different forms of α5β1[3,4] and comparison to purified full-length α5β1 in LMNG/CHS calculated from data in Figure 4A.

(D) Schematic of full-length α5β1 FRET reporters. Ectodomain reporters are identical except for truncation prior to the transmembrane domains (dashed lines).

(E) Conformation-specific Fabs used here.

(F) Affinity of TCO*-Lys and Cy3-tetrazine-labeled mutants for cyclic RGD peptide (cRGD, ACRGDGWCG) on transfected Expi293 β1 knockout cells from data in Figures S2E–S2G.

application by the actin cytoskeleton through adaptors such as talin that is resisted by extracellularly embedded ligand, rather than talin binding *per se*.

We focus here on integrin α5β1, the major receptor for fibronectin.[1,7] Fibronectin is ubiquitously expressed as fibrils in the extracellular matrix and as dimers in plasma. The Arg-Gly-Asp (RGD) motif recognized by 8 of 24 integrin heterodimers was first discovered in Fn3 domain 9 of fibronectin, where together with a synergy site in Fn3 domain 10 it is bound by α5β1. Study of how cells form nascent adhesions at their leading edges that mature to focal adhesions has centered on integrin α5β1 binding to fibronectin. Integrin α4β1 binds to a distinct region in fibronectin and to vascular cell adhesion molecule (VCAM).

Thermodynamic studies on integrins α5β1 and α4β1 have suggested that neither extracellular ligand binding nor talin binding is sufficient to stably maintain integrin activation. Integrin ensembles contain three overall conformational states: two low-affinity closed states, bent-closed (BC) and extended-closed (EC), and a high-affinity, extended-open (EO) state (Figure 1A). Bent/extended refers to the state of the knees and lower legs in the α and β subunits. Open and closed are generic terms for high- and low-affinity states, respectively, refer to the conformations of the β-subunit βI and hybrid domains, and happen to correlate with the amount of space between the upper α and β legs but not with the size of the ligand binding site (Figure 1A). The intrinsic ligand-binding affinity and ligand-binding kinetics of each conformational state of integrins α5β1 and α4β1 and the conformational equilibria linking these states are known (Figures 1B and 1C).[3,4,14] Utilizing such thermodynamic parameters, calculations have shown that when both extracellular ligand and an adaptor such as talin are bound, only the addition of cytoskeletal force that is resisted by ligand embedded in the extracellular environment can provide ultrasensitive regulation of integrin activation.[20] The calculated force required of ~2 pN is in the lower range of forces that single integrin molecules can exert on ligands.[21–23] However, as this model is based on thermodynamic equilibrium, to be valid, it requires rapid integrin conformational change and communication between ligand binding outside the cell and actin adaptor binding inside the cell.

Currently, there are no measurements that address whether integrin conformational change is initiated from inside or outside the plasma membrane; however, ligand-binding kinetics are consistent with the idea that extracellular ligand binding might initiate integrin activation. For both α5β1 and α4β1, the predominant bent-closed conformation binds ligand more rapidly than the extended-open conformation.[14]

Single-molecule fluorescence resonance energy transfer (smFRET) can resolve conformational dynamics.[24,25] smFRET has been successfully applied to receptors that span the membrane multiple times such as G-protein-coupled receptors (GPCRs), transporters, and neurotransmitter-stimulated channels as well as to trimeric viral proteins.[26–31] However, little is known about the dynamics of the large class of cell-surface receptors that, like integrins, have multi-domain ectodomains linked to single-pass transmembrane domains, including adhesion receptors, receptor tyrosine and serine/threonine kinases, receptor phosphatases, and JAK-STAT-linked receptors.

Here, we measure the conformational dynamics of integrin α5β1 using smFRET. Integrins are molecular machines with parts that undergo large, ~100 Å movements[2]; however, we believed

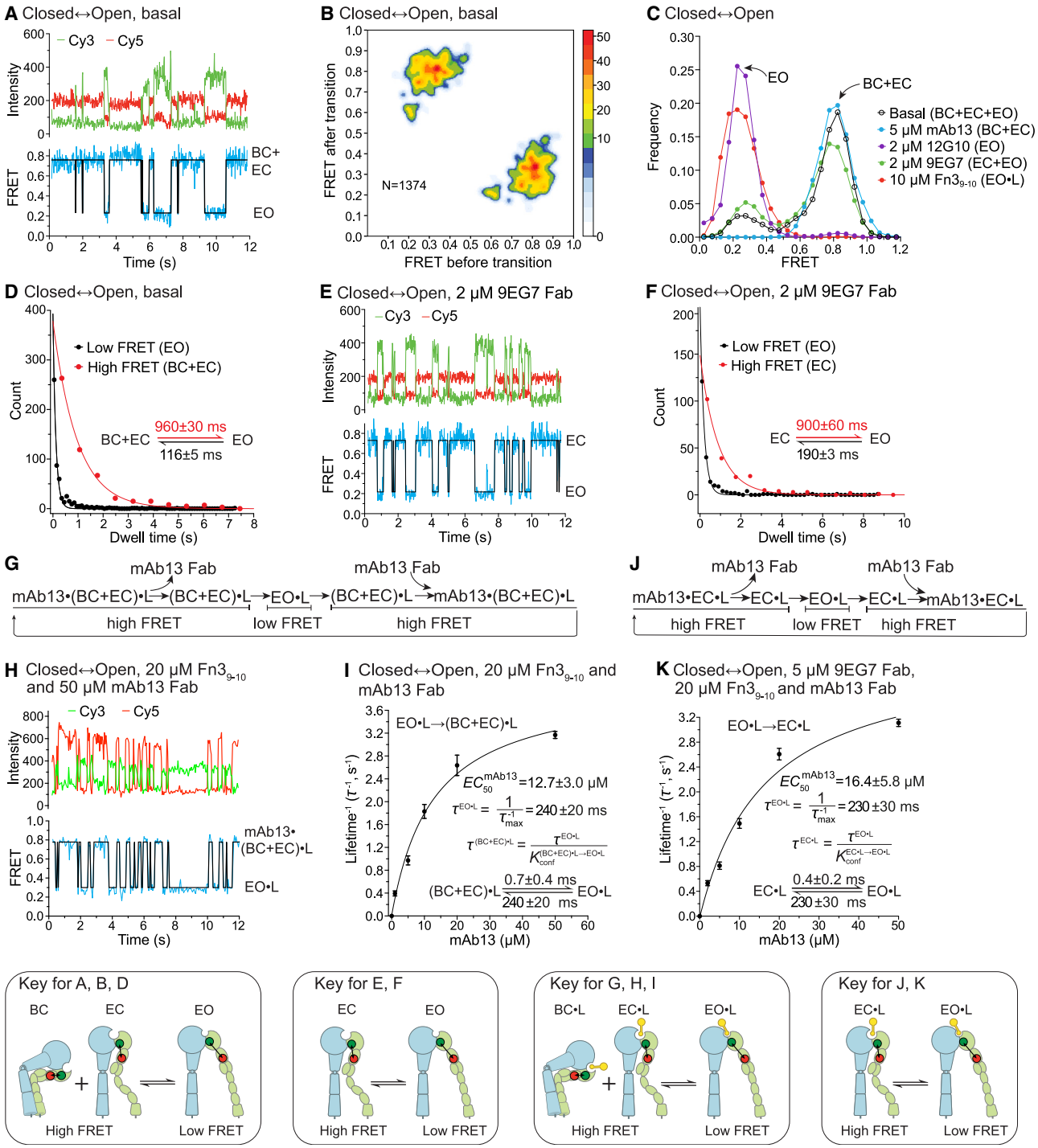

Figure 2. Conformational transition rates in the α5β1 ectodomain Closed↔Open reporter

(A, D, H) Representative time traces with fluorescence intensity (top) and FRET efficiency (bottom) with hidden Markov model fits (black) to data (cyan).

(B) Transition density plot under basal conditions (1,374 state-to-state transitions from 168 single molecule traces).

(C) Single-molecule FRET efficiency histograms from the number of molecules shown in Table S1.

(D and F) Dwell time distributions of FRET states with single-exponential fits. The lifetimes here and elsewhere denote the inverse of the rate of transitions for the associated arrows and would be the average lifetime of the originating state when no other reaction from the state is allowed.

(G and J) Scheme for measuring the dwell time of the EO•L state in the absence (G) or presence (J) of extension-stabilizing 9EG7 Fab.

(legend continued on next page)

that we could not understand this machine and truly appreciate its soul—its animating principle—until we saw it move. Indeed, we find multiple surprises. Integrin leg extension and headpiece opening are not independent of one another as originally envisioned but are concerted events. After ligand binding, the BC state transitions on a millisecond timescale directly to the EO state. Although intermediate between these two states in structure, the EC state is not a kinetic intermediate; however, it can be accessed from the EO state (Figure 1A). Counter to the dominant model in the field, we find that ligand binding initiates integrin activation and that talin has only a minor role in stabilizing the EO state. As integrins are important therapeutic targets in autoimmune disease and cancer, these findings have important implications for improving human health.[32,33]

RESULTS

Conformational dynamics of the α5β1 ectodomain

We use smFRET to measure conformational dynamics with both full-length integrins and ectodomain fragments because they each provide unique insights into integrin dynamics, owing to the different setpoints of their equilibria. When unliganded, intact integrins remain largely in the BC state, whereas the three states are relatively evenly distributed in ectodomain preparations (Figure 1C), allowing insight into their basal dynamics. To specifically label the α5β1 integrin with FRET-pairs, we used a pyrrolysine-based genetic code expansion system to incorporate *trans*-cyclooct-2-en-L-lysine (TCO*-Lys) at mutationally introduced pairs of amber codons.[34] Co-expressing a dominant-negative eukaryotic release factor 1 mutant lowered termination at amber codons and enhanced readthrough.[35] Single amber mutations were first tested for expression and click chemistry labeling efficiency with tetrazine-functionalized Cy3 or Cy5.[36,37] Paired amber mutations stochastically labeled with Cy3 and Cy5 were then tested for good separation between the high and low FRET states and photostability. To obtain our 2 FRET reporters, 26 single and 14 double amber mutations were tested before finding the best combinations (Figures 1D and S1A–S1C). Our two reporters had ligand-binding affinities near wild-type (Figures 1F and S2E–S2G). An average of 104 single-molecule fluorescence time traces were analyzed in the 64 single-molecule experiments in this study (Table S1).

We used antigen-binding antibody fragments (Fabs) to stabilize integrin α5β1 in specific conformations. Concentrations were at least 100-fold higher than EC_{50} values previously determined for the α5β1 ectodomain and, in the case of intact α5β1 in detergent, for energetically similar intact α5β1 on the cell surface[3] (Figure 1C). Fab concentrations differed for ectodomains and full-length integrins; for example, the higher stability of the BC state in full-length α5β1 (Figure 1C) required a higher concentration of extension-stabilizing Fab 9EG7.

With the α5β1 ectodomain, the Closed↔Open reporter (Figures 1D and S1D) showed frequent transitions between high (∼0.8) and low FRET (∼0.3) states (Figures 2A and 2B). At any one time, more single molecules were in the high FRET state with the headpiece closed (BC+EC) than the low FRET state with headpiece open (EO, Figure 2C), confirming previous thermodynamic ensemble measurements.[3] Fab mAb13 specific for the closed conformations stabilized all single molecules in high FRET (BC+EC states) and Fab 12G10 specific for the open conformation stabilized molecules in the low FRET (EO state), validating assignment of conformational states (Figure 2C). The kinetics of (BC+EC)↔EO transitions from fits of the FRET time traces to a two-state hidden Markov model (HMM)[38] (Figure 2A) were well fit to single exponential decay (Figure 2D). The lifetime of BC+EC states were longer than of the EO state (Figure 2D), agreeing with the lower population of the ectodomain EO state (Figure 1C).

In the presence of extension-stabilizing 9EG7 Fab, more single molecules were in the EC than EO state (Figure 2C). Kinetics were well fit to single exponential decay and showed that the lifetime of the EO state was shorter than the EC state and both were sub-second (Figures 2E and 2F). Similar results were obtained with extension-stabilizing Fab 8E3 and at different Fab concentrations (Figures S3A–S3C).

Addition of saturating ligand, a fibronectin fragment containing Fn3 domains 9 and 10 ($Fn3_{9-10}$), showed exclusively low FRET of the EO•L state (Figure S3D), suggesting that the high FRET (BC+EC)•L state was too short-lived to detect at 50 ms/frame rate as used here. Therefore, to temporarily stabilize the (BC+EC)•L state when it appeared, we added varying concentrations of closure-specific mAb13 Fab, to mark the beginning and end of the low FRET EO•L state (Figures 2G and 2H). The lifetime of the low FRET EO•L state at saturating mAb13 Fab concentrations was 240 ms (Figures 2I, S3E, and S3F). With extension-stabilizing Fab, the EO•L state lifetime was similar (Figures 2J, 2K, and S3G–S3H). Using the conformational equilibrium between the closed and open liganded states[3] (Figure S3I), we used the measured lifetime in one direction to calculate the lifetime in the opposite direction, from (BC+EC)•L to EO•L or from EC•L to EO•L, as ∼0.5 ms (Figures 2I and 2K). Thus, ligand binding to the closed ectodomain increased its transition rate to the EO state 2,000-fold; from a lifetime of ∼1 s in the absence of ligand (Figures 2D and 2F) to ∼0.5 ms when bound to ligand.

The Bent↔Extended reporter (Figures 1D and S1D) showed frequent transitions between high FRET (∼0.60) and low FRET (∼0.35) states (Figures 3A and 3B). Fabs that stabilized the extended conformations or the EO conformation, as well as ligands that stabilized the EO state, gave low FRET, and the basal BC+EC+EO states and Fab that stabilized the closed (BC+EC) states had predominately high FRET (Figure 3C), validating the

(I and K) EO•L transition rates as a function of mAb13 Fab concentration (Figures S3E–S3H) with dose-response fit to mAb13 Fab EC_{50} and maximum transition rate. The concentration of mAb13 Fab was as high as possible considering its solubility and occupation of 60% of the imaging volume by oxygen scavenging buffer. Errors are standard errors from nonlinear least square fits; lifetimes calculated using the thermodynamic cycle (Figure S3I) show errors from error propagation. Conformational transition rates were determined using at least two independent samples and imaging chambers. All transitions, from the number of single-molecule traces shown in Table S1, are included in results.
See also Figure S1.

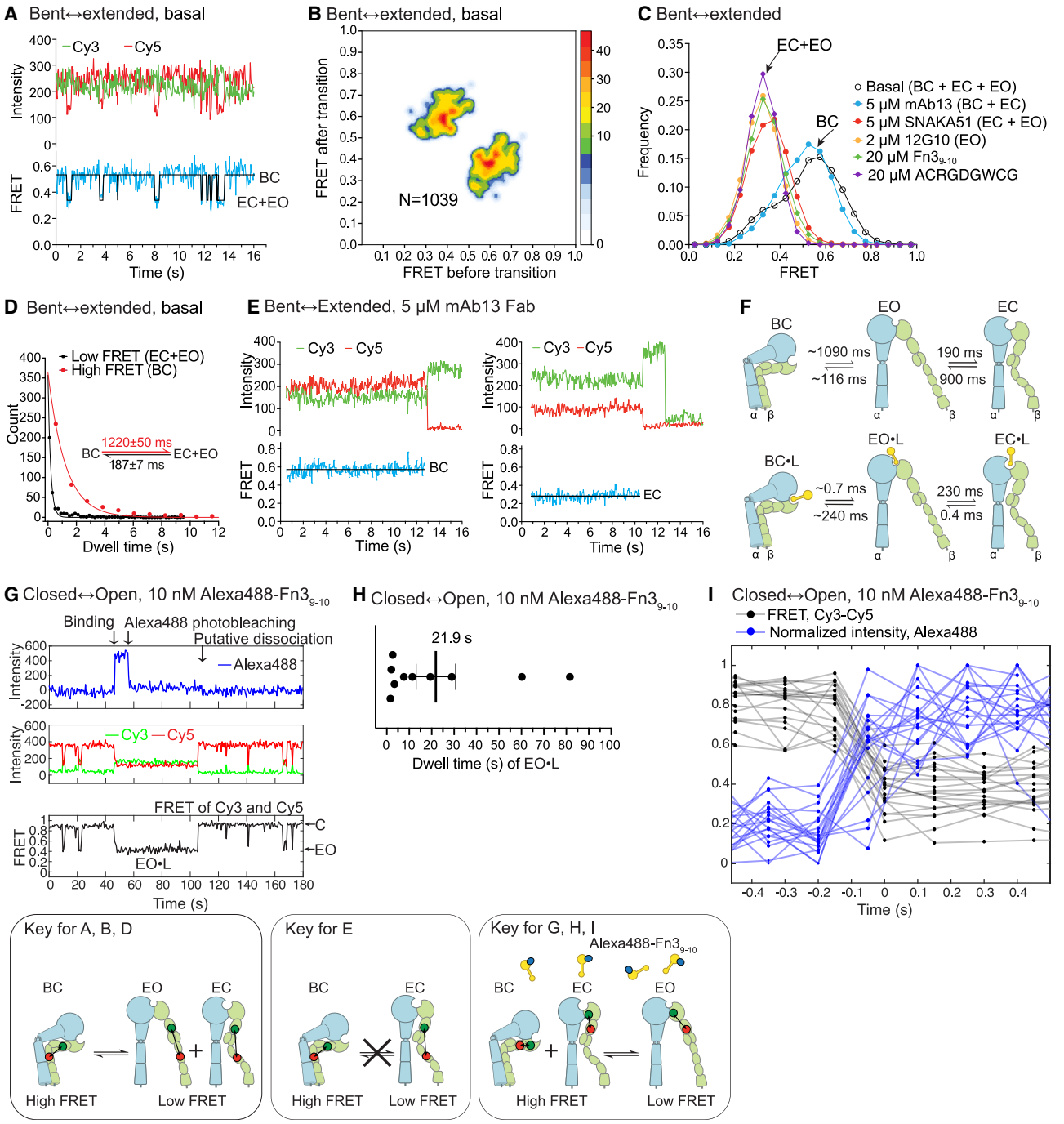

Figure 3. Conformational transitions in the α5β1 ectodomain Bent↔Extended reporter and coupling to ligand binding

(A) Representative time trace.

(B) Transition density plot under basal conditions.

(C) Single-molecule FRET efficiency histograms.

(D) Dwell time distributions of FRET states with single-exponential fits. Errors from nonlinear least square fits are as detailed in Figure 2 legend.

(E) Representative time traces showing molecules trapped in BC (left) and EC (right) states.

(F) The sequence and rates of conformational transitions in unliganded and liganded α5β1 ectodomain.

(G–I) 3-color experiments on the α5β1 ectodomain Closed↔Open reporter with 10 nM Alexa 488-Fn3$_{9-10}$.

(legend continued on next page)

reporter. The basal lifetimes for the bent and extended states were second and subsecond, respectively (Figure 3D). In the presence of 20 μM $Fn3_{9-10}$, the Bent↔Extended reporter showed only low FRET (Figure S3K), suggesting that the lifetime of the high FRET BC•L state was very short, consistent with the very short lifetimes of the (BC+EC)•L states observed using the Closed↔Open reporter. The same result was obtained with a cyclic RGD peptide (cRGD, ACRGDGWCG, Figure S3L).

Closure-stabilizing Fab mAb13 stabilized single α5β1 ectodomains in high and low FRET states in the relative proportions expected from thermodynamic measurements of their populations in the BC and EC states, respecitively[3] (Figure 3C). However, these single molecules were trapped either in the high FRET state or in the low FRET state (Figure 3E). None of the 124 time traces, which extended ∼10 to 30 s prior to photobleaching, showed a molecule with high FRET transiting to low FRET or a molecule with low FRET transiting to high FRET. Because Fab mAb13 binds to an epitope near the ligand binding pocket, we also tested another closure-stabilizing Fab, SG19, which binds distal to the ligand-binding site (Figure 1E), and obtained the same result (Figure S3M). Therefore, BC and EC states cannot interconvert when headpiece opening is not allowed. Integrin structures suggest that interlock of the lower β leg with both the upper and lower α leg in the BC state prevents extension and is relieved by opening (discussion).

The lifetimes of the α5β1 ectodomain open and extended states, 116, 190, and 187 ms, are similar, as are the lifetimes of the ectodomain closed and bent states, 960, 900, and 1,220 ms (Figures 2D, 2F, and 3D). The similar kinetics of integrin opening and extension and of bending and closing along with the lack of detectable transitions between the BC and EC states in the presence of closure-stabilizing Fabs suggest that opening and extension of the BC state are concerted conformational transitions, that closing and bending are also concerted, and that the EC and BC states are not directly reachable from one other (Figure 3F). Thus, while the EC state is structurally intermediate in conformation between the BC and EO states (Figure 1A), it is not in the kinetic pathway between these states. Instead, the EC state is readily accessible from the EO state (Figures 2E, 2F, 2J, 2K, and 3F).

To directly examine the relationship between ligand binding to integrin α5β1 and conformational change, we performed 3-color single-molecule measurements using Alexa 488-labeled $Fn3_{9-10}$ in solution together with the Closed↔Open ectodomain reporter immobilized on the imaging slide. We sequentially illuminated Alexa 488, Cy3, and Cy5 each for 200 ms (Figures 3G and 3H) or 50 ms (Figure 3I) and simultaneously acquired emission intensity. All observed $Fn3_{9-10}$ binding events coincided with the transition to low FRET EO state within our temporal resolution (Figure 3I), confirming that ligand binding induced integrin activation to EO•L. $Fn3_{9-10}$ remained bound for ∼22 s (Figure 3H), as determined from averaging events in which the low FRET state persisted after Alexa 488 photobleaching (Figure 3G) or in which loss of $Fn3_{9-10}$ fluorescence and return of the high FRET state coincided (Figure S3N). Using previously measured kinetics of $Fn3_{9-10}$ dissociation from α5β1[14] and conformational transition kinetics measured here, we calculated the time required for ligand dissociation from α5β1. We used the conformational lifetime of the EO•L state of 240 ms (Figure 2I), its dissociation lifetime of ∼200 min[14] (Figure 1B), the conformational lifetimes of the BC•L and EC•L states of ∼0.7 ms which interconvert with EO•L (Figure 2I), and the BC•L and EC•L dissociation lifetimes of 700 ms[14] (Figure 1B). The calculated ligand-binding lifetime of the α5β1 ectodomain after initial formation of EO•L is 25 s (Figure S4K), in agreement with the average lifetime of ∼22 s (Figure 3H).

Conformational dynamics in full-length α5β1

To measure conformational transition rates in full-length α5β1, we solubilized it in the nonionic detergent lauryl maltose neopentyl glycol (LMNG) mixed with an acidic cholesterol ester, cholesterol hemisuccinate (CHS), which preserves the structure of G-protein coupled-receptors and ion channels and has a bicelle-like architecture.[39–41] Phosphatidylinositol phosphate (PIP) analogs with octanyl groups, 08:0 PI(4,5)P2 and 08:0 PI(3,4,5)P3, were also successfully incorporated into the LMNG/CHS micelle as shown by a large increase in micelle size (Figure S4A). We first measured bulk properties of purified full-length α5β1 (Figures S2A and S2B).

Affinity for cRGD peptide of the α5β1 ensemble in LMNG/CHS and stabilization of specific conformations with Fab (Figures 4A and S4C) was used to calculate the population of each α5β1 state.[3] The BC and EO states were 98.7% and 0.5% populated, respectively, not far from the populations of intact α5β1 on the cell surface of 99.8% and 0.2%, respectively[3] (Figure 1C), showing that our condition recapitulates the integrin conformational equilibrium on the cell surface. Moreover, the presence of PIP2 or PIP3 analogs in LMNG/CHS had little influence on the α5β1 full-length conformational equilibrium (Figure S4B).

Bent↔Extended and Closed↔Open reporters (Figures 1D and S2D) showed single full-length α5β1 molecules predominantly in the high FRET bent and closed conformations, respectively (Figures 4B and 4C). A minority of time traces showed a single transition to the extended or open conformations (Figures 4D and 4E). The rarity of these events agreed with the stability of full-length α5β1 in the BC state (Figures 4A–4C). In contrast, stabilization of extension with Fab 9EG7 revealed frequent transitions between the EC and EO states (Figure 4F) that had lifetimes (Figure 4G) very similar to those determined with the ectodomain (Figure 2F). Together, the rarity of extension or opening of intact α5β1 and its facile conversion in the presence of extension-stabilizing Fab between the EC and EO states with kinetics similar to those with the ectodomain suggest that the α and β-subunit transmembrane domains are associated in

(G) Example time trace of Alexa 488-$Fn3_{9-10}$ (top) and FRET reporter (middle and bottom). Alexa 488, Cy3, and Cy5 were sequentially illuminated (200 ms/frame).
(H) Dwell times collected for the EO•L state (mean ± S.E., 10 single molecules from 24 movies, 8 independent measurements).
(I) FRET change upon Alexa 488-$Fn3_{9-10}$ binding. Twenty traces from 15 movies (5 independent experiments) were aligned to the first frame of EO•L state (50 ms/frame).
See also Figures S1 and S3.

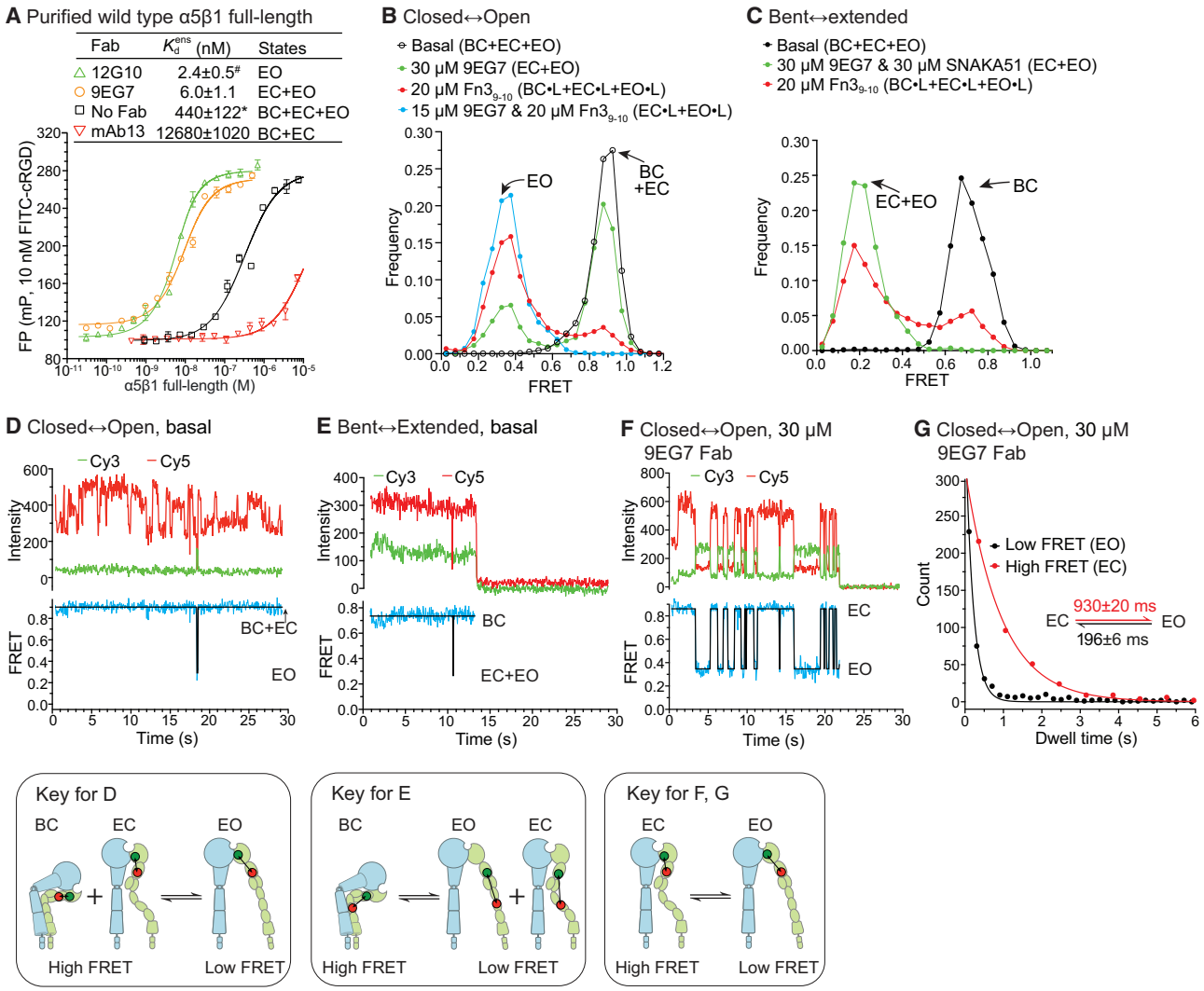

Figure 4. Affinities and conformational transition rates of full-length α5β1 in LMNG/CHS

(A) Upper: Affinity of wild-type full-length α5β1 for FITC-cRGD in specific conformational states measured using bulk fluorescence polarization (FP) assays in the presence of Fabs as indicated. Errors in affinity values are SE from nonlinear least square fits except value with "*" is difference from the mean from two experiments on different days and value with "#" is global fit from three different datasets with different FITC-cRGD concentrations accounting for the effect of high-affinity binding on ligand depletion (Figure S4C). Lower: Representative data; errors in datapoints are standard deviations of triplicates.

(B and C) FRET histograms.

(D and E) Time traces showing rare transitions.

(F) Representative time trace.

(G) Dwell time distributions of FRET states with single-exponential fits. Errors are standard errors from nonlinear least square fits, as detailed in Figure 2 legend. See also Figures S2 and S6.

the BC state, but not associated in the EC and EO states, as previewed in Figure 1A.

Ligand binding greatly accelerated headpiece opening and leg extension of intact α5β1 as detected via high to low FRET transitions (Figures 5A–5D). The transitions back to the high FRET states did not depend on Fn3$_{9-10}$ concentration from 2 to 20 μM (Figures 5E, S4E, and S4G), consistent with saturation of the EO state with Fn3$_{9-10}$ given its K_d of ~1 nM.[3] In contrast, transition from high FRET BC+EC or BC states in the Closed↔Open or Bent↔Extended reporters, respectively, to the low FRET states was dependent on Fn3$_{9-10}$ concentration with EC_{50} values of 10 μM (Figure 5F), consistent with 9–12 μM affinities of the BC and EC states for Fn3$_{9-10}$.[3] The millisecond timescale for conversion of the BC state to the EO state after ligand binding provides a facile pathway for integrin activation (Figure 5F). The similar lifetimes of full-length α5β1 bound to ligand for the Closed↔Open reporter in the BC•L state and for the Bent↔Extended reporter in the BC•L+EC•L states (essentially indistinguishable at 63 and 67 ms, Figure 5F) suggest that opening and extension are concerted (Figure 5H). Lifetimes of the ligand-bound extended and open states were also similar (Figure 5E). Given the negligible population of the EC•L state in the

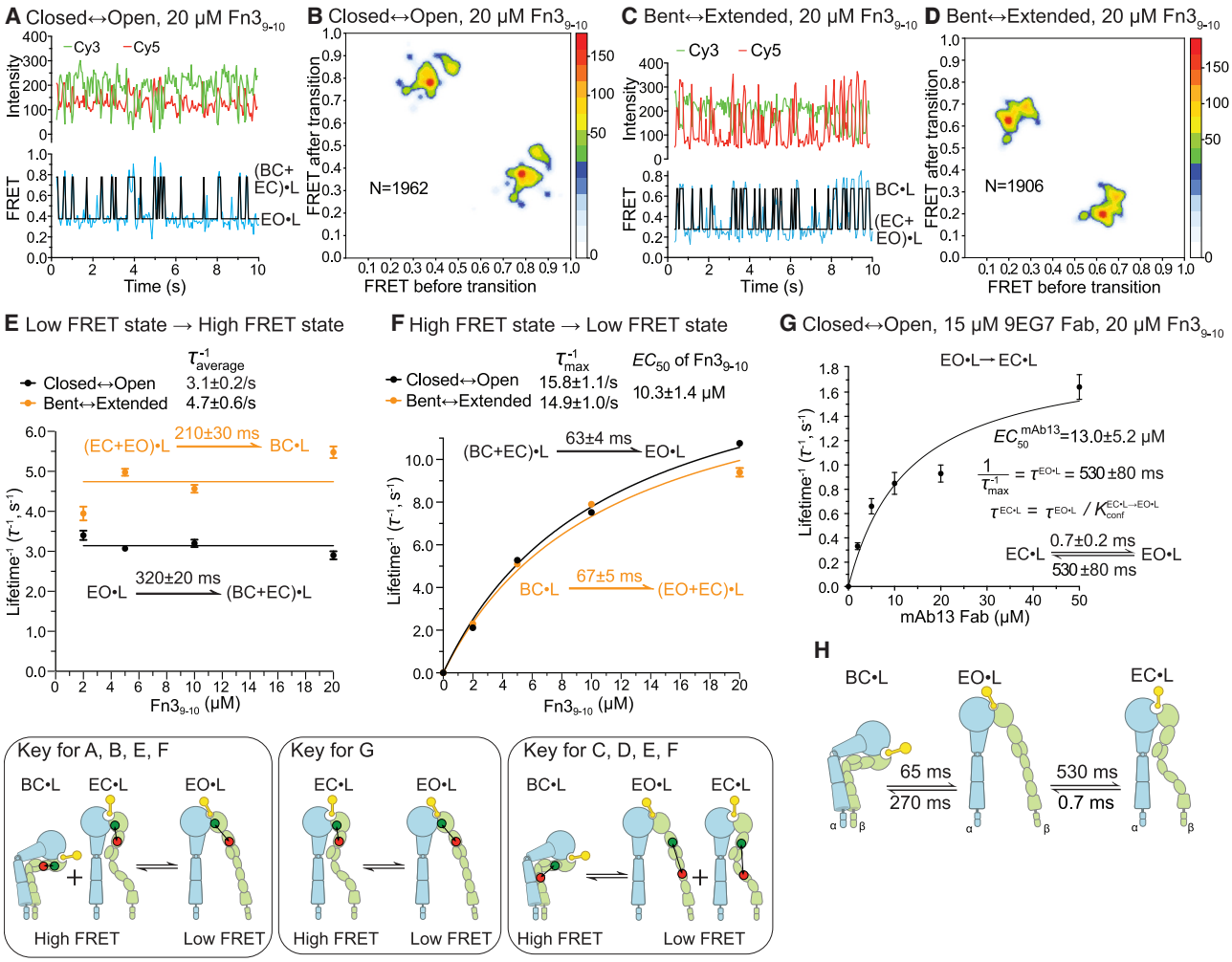

Figure 5. Conformational transition rates of liganded α5β1 full-length in LMNG/CHS

(A and C) Representative time traces.

(B and D) Transition density plots.

(E) Low to high FRET transition rates of FRET reporters at different $Fn3_{9-10}$ concentrations do not show concentration dependence as expected because concentrations are far above the K_d for the EO state (Figure 1B) and are fitted with horizontal lines.

(F) High to low FRET transition rates of FRET reporters as a function of $Fn3_{9-10}$ concentration with dose-response curve fits (maximum rate and EC_{50} of $Fn3_{9-10}$ concentration, with shared EC_{50}).

(G) EO•L to EC•L transition rate as a function of mAb13 Fab concentration (Figures S4H–S4J) with a dose-response fit (mAb13 Fab EC_{50} and maximum transition rate).

(H) The sequence of ligand induced conformational transitions in full-length α5β1.

Errors are as described in Figure 2 legend.

See also Figures S2 and S6.

ensemble in the presence of saturating ligand (Figure 1C) and therefore its negligible contribution to lifetime measurements, we may conclude that closing and bending of EO•L to form BC•L are also concerted (Figure 5H).

We also measured the lifetimes of EC•L and EO•L in the presence of saturating 9EG7 Fab and $Fn3_{9-10}$ using the full-length Closed↔Open reporter. As with the ectodomain, the EC•L state of full-length α5β1 was short lived, and we therefore titrated in mAb13 Fab to stabilize the EC•L state and mark the beginning and end of the EO•L state (Figures 2J and S4H–S4I). Using the lifetime of 530 ms determined for the EO•L state (Figure 5G) along with the conformational equilibrium[3] (Figure S3I), we calculated the lifetime of 0.7 ms for the EC•L state.

Regulation of α5β1 activation by talin1

We first used bulk assays to measure the effect of the integrin-binding head domain of talin1[13,42] on ligand binding of full-length α5β1. Talin1 head domain slightly enhanced ligand binding by full-length α5β1 in both the presence and absence of the PIP2 analogue 08:0 PI(4,5)P2 (Figures 6A, S5A, and S5B). In contrast, ligand binding by full-length α4β1 was slightly enhanced by the talin1 head only in the presence but not in the absence of 08:0

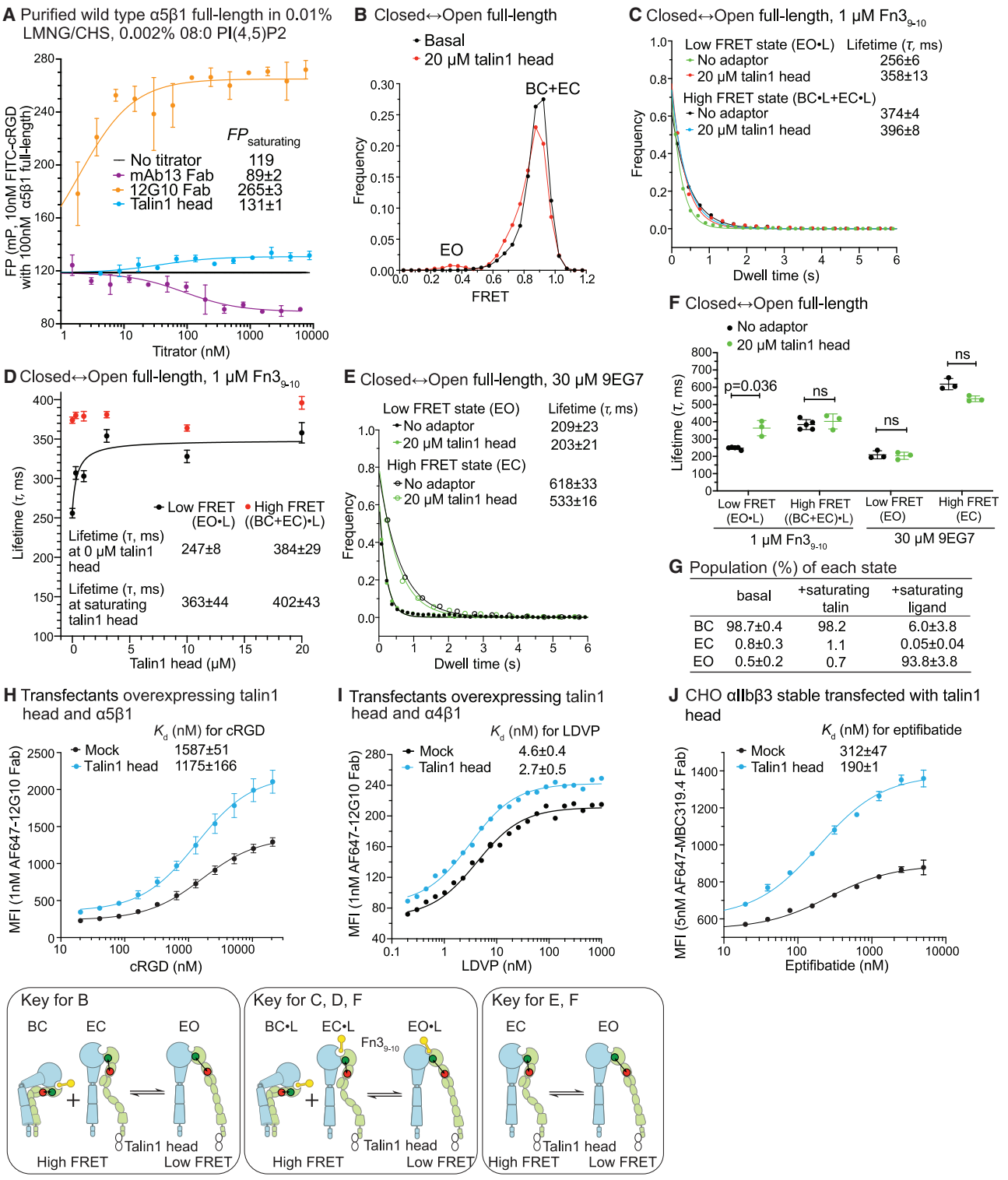

Figure 6. Effect of talin on integrin activation

(A) Effect of talin1 head compared to conformation-specific Fab on full-length α5β1 binding to FITC-cRGD in FP assays. Saturating FP value and its error (SE) are from dose-response curve fit of triplicates.

(B–F) Effect of talin1 head on full-length Closed↔Open reporter.

(B) FRET efficiency histograms.

(legend continued on next page)

PI(4,5)P2 (Figure S5C). The reason for these differences between α5β1 and α4β1 are unclear. However, our results with α5β1 are consistent with the role of PIP2 in releasing the head in intact talin from autoinhibition by the rod domain[43,44] and with the ability of talin1 head to bind to integrin αIIbβ3 in nanodiscs in the absence of PIP2.[45]

Single-molecule measurements of full-length α5β1 with the Closed↔Open reporter showed that 20 μM talin1 head slightly increased the population of the low FRET open conformation (Figure 6B) but much less than 20 μM $Fn3_{9-10}$ (Figure 4B). Observation of the low FRET state with talin was too infrequent to measure its lifetime. Therefore, we measured the effect of talin1 head on the Closed↔Open reporter in the presence of 1 μM $Fn3_{9-10}$. The lifetime of the low FRET state (EO•L) in 1 μM $Fn3_{9-10}$ of 250 ms was increased by talin1 head to 360 ms whereas the lifetime of the high FRET state was not affected (Figures 6C, 6D, 6F, and S5D). Thus, talin1 head binding stabilizes the EO•L state and increases its lifetime by ∼35%. To further check whether talin1 head has preference for the EO over the EC state, we employed 30 μM 9EG7 Fab to stabilize the full-length α5β1 Closed↔Open reporter into the two extended states (Figure 6E). Neither the EO state lifetime nor the EC state lifetime was markedly influenced by talin1 head (Figures 6E and 6F). These results suggest that the cytoplasmic tail of the β subunit is similarly accessible to talin in the EO and EC states, consistent with evidence above that the transmembrane domains are separated in both states, and suggest that the BC state with its associated α- and β-transmembrane domains cannot bind talin. As talin1 head binding only increases the lifetime of the extended states by 35%, the population of EO state remains low: 0.5% vs. 0.7% before and after adding talin1. In contrast, saturating ligand binding increases the population of EO state from 0.5% to 94% (Figure 6G).

Measurements on cells in suspension showed similarly slight enhancement of ligand-binding affinity by talin1 head overexpression. Co-transfection of Expi293 cells with integrin α5β1 and the EGFP-talin1 head (Figure S5E) increased affinity for cRGD by 1.4 ± 0.2-fold compared to the EGFP control (Figure 6H). Co-transfection of Expi293 cells with the integrin α4β1 and the EGFP-talin1 head (Figure S5F) increased α4β1 affinity for the peptidomimetic ligand, MUPA-LDVPAAK (LDVP),[46] by 1.7 ± 0.3-fold (Figure 6I). Previously, the ability of the talin1 head domain to activate integrin αIIbβ3 was inferred from increased binding to PAC-1,[45,47] an IgM that reacts with an activation-induced conformational epitope in the integrin ligand binding site.[48] Using a previously reported αIIbβ3 CHO stable transfectant,[47] we confirmed that transient overexpression of talin 1 enhanced binding of PAC-1 IgM (Figure S6A); however, the previously reported "activation index" was not robust in our hands (Figure S6B). The PAC-1 assay is done out of equilibrium with two sets of washes and is also amplified with a secondary anti-IgM antibody. To measure true αIIbβ3 affinity for ligand, we used eptifibatide, a therapeutically approved RGD-mimetic that binds to the open conformation of αIIbβ3.[33] Talin1 head transfection increased affinity of αIIbβ3 for eptifibatide by 1.6 ± 0.3-fold (Figure 6J).

DISCUSSION

Previous work on integrins α5β1 and α4β1 defined the affinities and populations of the BC, EC, and EO states in headpiece and ectodomain fragments and on cell surfaces[3,4] (Figures 1B and 1C). Single-molecule measurements here independently validated the presence of integrins in discrete conformational states but have taken us much further by revealing the timescales and pathways for conformational interchange (Figure 7A). Ensemble affinity measurements on intact α5β1 in LMNG/CHS with or without 08:0 PI(4,5)P2 showed that the populations of the BC, EC, and EO states were similar to those previously determined for intact α5β1 on cell surfaces. Therefore, our single-molecule observations on intact α5β1 are likely to approximate integrin single-molecule kinetics on intact cells. Frame rate and temperature had only minor effects (Figures S6C–S6G).

The results here should also hold for other integrins with BC, EC, and EO conformations, as exhibited by many representatives of the 22 of 24 integrin heterodimers that contain β-subunits with talin and kindlin binding sites.[1,50] Clustering of integrins on cells occurs when they bind extracellularly embedded ligands and the cytoskeleton, and form a variety of assemblies including nascent and focal adhesions, filopodia-tip adhesions, invadosomes, and reticular adhesions.[51] While the cadherin class of adhesion molecules pack closely with one another on cell surfaces, as modeled by packing in crystals,[52] there is no similar

(C and E) Dwell time distributions of the low and high FRET states with single-exponential fits.

(D) Dependence of the lifetimes of the low and high FRET states on the concentration of talin1 head in the presence of 1 μM $Fn3_{9-10}$. Lifetime of the low FRET state at each talin1 head concentration (Figure S5D) was fitted to dose-response curve to determine the lifetime in the absence of and at saturating concentration of talin1 head.

(F) Lifetimes of the low and high FRET states in various conditions. *p* values are from unpaired two-tailed Student's t test (n = 3 to 5 independent experiments). ns: $p > 0.05$.

(G) Population of each state in full-length α5β1. Data are calculated from that in Figure 4A, the thermodynamic cycle (Figure S3I), and the 1.35-fold increase of the EO•L state lifetime with saturating talin 1 head (as shown in C–F). Errors are propagated from errors in binding affinities.

(H–J) Effect of talin1 head transfection on integrin monomeric ligand affinity in intact cells.

(H and I) Affinity of α5β1 for cRGD (H) and α4β1 for LDVP (I) in transfected Expi293 cells measured by enhanced binding of 1 nM AF647-12G10 Fab.

(J) Affinity of αIIbβ3 for eptifibatide on CHO αIIbβ3 stable transfectants measured by enhanced binding of 5 nM AF647-MBC319.4 Fab. Mean fluorescence intensity (MFI) of AF647 in $EGFP^+$ cells was fitted to a dose-response curve with three parameters: background MFI, maximum MFI, and EC_{50}. EC_{50} value is identical to K_d.

Errors in (A)–(E) are SE from nonlinear least square fits, as detailed in Figure 2 legend; errors in (H)–(J) are difference from the mean of two independent measurements.

See also Figures S2 and S6.

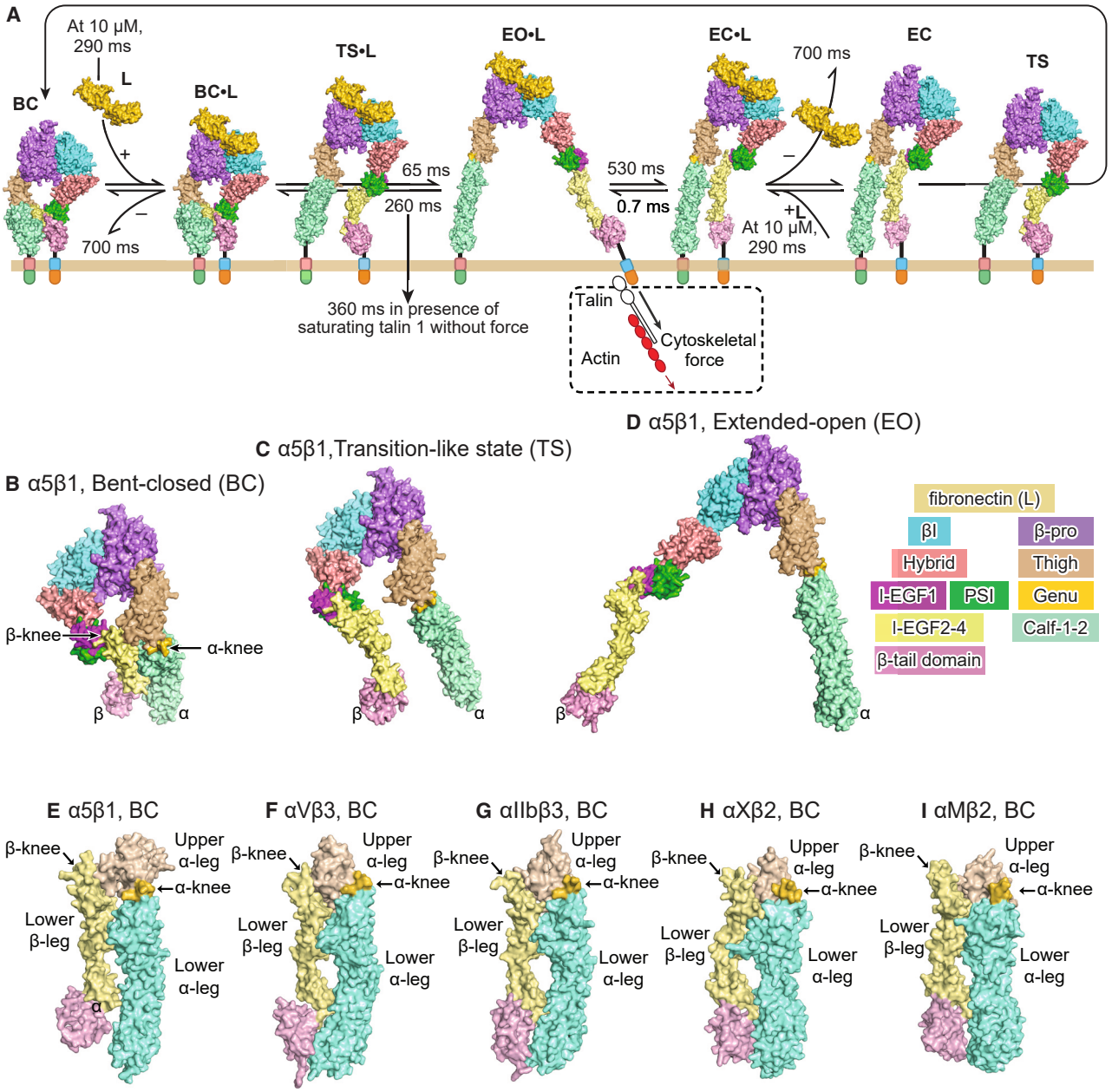

Figure 7. The pathways for integrin conformational change in the integrin α5β1 machine and the structural requirement for concerted integrin headpiece opening and extension at the knees

(A) The pathway of α5β1 activation. Lifetimes (timescales) for ligand binding and dissociation[14] and conformational change are shown at 22°C. The transition like state (TS) is described below in (C).

(B) In bent-closed α5β1 (PDB: 7nxd), interlock at the α and β subunit knees prevents extension but not headpiece opening.

(C) Movement of 1/3 along the trajectory toward open α5β1[49] separates the knees, but also breaks all other α and β subunit leg contacts, destabilizing the bent conformation. Therefore, 1/3 opening and 1/3 extension are shown to simulate a transition-like state.

(D) Extended-open α5β1 is modeled using open, ligand-bound α5β1 (PDB: 7nxd), with its disordered lower legs replaced with the legs from the bent-closed structure (STAR Methods).

(E–I) Leg structures of bent-closed integrins α5β1 (PDB: 7nxd, E), αVβ3 (PDB: 4g1m, F), αIIbβ3 (PDB: 3fcs, G), αxβ2 (PDB: 5es4, H), and αMβ2 (PDB: 7usm, I).

evidence that clusters of integrins have specific inter-molecular associations.[53] Thus, we believe that cell surface clusters of integrins can be viewed as collections of single molecules that behave as described here.

A major question in the integrin field has been the sequence of events in integrin activation and whether the initiating events come from inside or outside the cell. Our results show that the key initiating event is extracellular ligand binding. Following

ligand binding to the BC state, it converts to the extended open conformation in ~65 ms (Figure 7A). In the absence of ligand, BC state conversion to the EO state was sluggish, taking ~30 s (Figure S6C). Furthermore, the postulated talin-mediated activation of integrins would hinder ligand binding: the high-affinity EO states of α5β1 and α4β1 bind ligand 5- and 40-fold more slowly than their low-affinity closed states, respectively.[14] In contrast to ligand, binding of the talin1 head to the integrin had no measurable effect on conversion of the BC to EO state, although it did decrease the rate of EO state conversion to the BC state by 1.3-fold. The subtle but significant effect of talin on integrin activation observed with single molecules was validated with live cells. Transfection with the talin1 head domain increased integrin α5β1, α4β1, and αIIbβ3 cell surface affinities for monomeric ligands by 1.4- to 1.7-fold. We confirm a role for talin in integrin activation[9,54]; however, talin effects on integrin affinity are lesser than expected from the 3.5-fold increase in activation index reported using multimeric PAC-1 IgM[47] and far less than the 2,000-fold increase in affinity between the closed and open integrin states. Compared to fibronectin, talin recruits a much smaller proportion of integrins to the EO state (Figure 6B compared to 4B), does not measurably bind to and activate the BC state, and does not stabilize the EO over the EC state. We conclude that extracellular ligand binding (outside-in signaling) is the key event that initiates integrin activation.

Even combined binding of fibronectin and talin was insufficient to maintain α5β1 integrin activation, because its complex with ligand and talin transitioned back to the BC state in ~360 ms (Figure 7A). Our results imply that tensile force is also required to stably populate integrins in the extended-open conformation, supporting previous thermodynamic calculations.[20] Conformation-specific antibodies specific for the extended and open integrin conformations bind little to activated cells in suspension, but well to activated cells adherent to ligands on substrates, in which integrins can resist cytoskeletal force.[16] Fabs that stabilize the closed conformation block adhesion through α5β1.[55] Together, this prior literature and our results imply that it is not talin binding *per se* but rather force transmission through talin that is required for integrin activation.

Conformational dynamics here of intact integrins and ectodomain fragments provided complementary information. Unliganded full-length integrins rarely visited the open and extended conformations; however, ectodomains had faster dynamics. The ectodomains allowed the discovery that closure-stabilizing Fabs binding to distinct epitopes in the βI and hybrid domains each blocked transitions in both directions between the BC and EC states. Association of integrin α and β subunits at their TM and cytoplasmic domains in the BC state and not the EO and EC states (Figure 1A) is supported here by the similar kinetics of conformational change between EO and EC states in ectodomain and full-length integrin forms and by the much higher rate of ectodomain than full-length integrin extension upon ligand binding (Figures 3F and 5H), in agreement with thermodynamic measurements.[3] Together with our finding that talin1 head did not alter the kinetics of EO and EC state interconversion, these results are consistent with the model that talin binds to the β-subunit cytoplasmic domain when the integrin α and β subunit TM and cytoplasmic domains are separated.[54]

Activation of actin polymerization in white blood cells and platelets coincides with integrin activation.[19] Integrin activation in tissue cells is closely linked to actin polymerization and retrograde flow.[7] In this context, what is the meaning of our observations? On living cells, ~99% of unliganded integrins are in the bent-closed conformation and the two closed conformations bind ligand more quickly than the extended-open conformation.[14] Integrin activation thus starts from the outside with ligand binding to the BC state (Figure 7A). This outside-in signaling induces millisecond-scale concerted conformational change to the EO•L state. Calculations using the kinetic constants for α5β1 EO•L state conformational transitions with the EC•L and BC•L states and fibronectin dissociation from these states (Figure 7A) show that the apparent lifetime of the EO•L state is 4.6 s (Figure S4K). Given the high μM concentration of talin in the cytosol[56] and assuming that PIP2 concentrations in the membrane are not rate limiting for stimulating talin opening,[43,44] persistence of the EO•L state for 4.6 s is a reasonable timescale for association of kindlin, talin, and the actin cytoskeleton and cytoskeletal loading of force on integrins at 1 pN/s.[57] Transmission of >2 pN of tensile force across the ligand-integrin-adaptor complex would then stabilize the EO•L state[20] and promote the formation of nascent adhesions, which are estimated to contain an average of 6 α5β1 integrins.[58] Thus, outside-in signaling (ligand binding to integrins) would initiate integrin activation, and inside-out signaling (integrin binding to talin, kindlin, and the actin cytoskeleton) would stabilize the EO•L state rather than inducing it. The ~65 ms timescale of BC•L transition to the EO•L state with its separated α and β subunit TM domains enables rapid coordination of events outside the cell with intracellular activation of talin and actin polymerization—both of which are driven by PIPs—providing a seamless method for activating integrins at cellular locations where extracellular ligand is available and actin and cytoskeletal adaptors are activated.

Despite the large length scales of conformational change in integrins, their transitions are fast. Transition rates measured in other cell surface receptors, which generally have multiple transmembrane domains, range from the microsecond to millisecond for ion channels,[30,59–61] millisecond to second for GPCRs,[28,62,63] and second to minute for neurotransmitter transporters.[29,64]

As discussed above, conformational transitions between the BC and EC states do not occur in the presence of Fabs specific for the closed conformation, showing that at least partial opening is required for integrin extension and bending. Furthermore, similar time scales are found for leg extension and headpiece opening (and of leg bending and headpiece closing) for the ectodomain fragment in the absence of ligand and for intact α5β1 in the presence of ligand. We conclude that extension and headpiece opening are concerted rather than independent movements. Thus, the extended-closed conformation is not on the pathway between the bent-closed and extended-open conformations (Figure 7A). In both partially bent α5β1[49] and more fully bent β2 and β3 integrins,[65–68] the α and β legs interlock (Figures 7B and 7E–7I). In the absence of partial opening, contact of both the upper and lower α legs with the lower β leg prevents mutual knee extension and either knee from extending alone. Headpiece opening in α5β1 swivels the upper β leg away from α by 66°[49] (Figure 7D). Even one-third of this opening breaks

all contacts between the α- and β-subunit legs that stabilize the bent conformation, permitting leg extension at the knees, as shown in a transition state-like structure between the BC and EO states that is 1/3 open and 1/3 extended (Figure 7C). Integrin structures thus provide a firm foundation for explaining our finding that opening and extension are concerted movements (Figure 7A). Ligand binding-triggered headpiece opening disrupts interfaces between the lower legs, and thus leg extension and opening are likely to occur together. In return of the EC state to the BC state, partial headpiece opening must also occur to allow the legs to nestle together (Figure 7A).

The extended-closed conformation readily interconverts with the extended-open conformation. Thus, although not on the pathway of integrin activation, the EC state may have an important role in ligand dissociation in the pathway of integrin deactivation (Figure 7A). This role may be particularly important in ligand dissociation in the presence of force, because tensile force would prevent ligand-bound integrins from converting back to the BC state.

Our study reveals that the material essence of integrins, the three-dimensional structures of their states, was insufficient to understand how integrins worked as machines. Comparisons of ligand binding and talin binding uncovered that the transition to the active EO state is induced on a rapid timescale by ligand. Separation of the TM domains of the two integrin subunits in the extended-open state transmits the signal into the cell that ligand is bound and permits talin binding. In contrast, talin had a minor stabilizing effect on the active state but did not induce it. Watching the integrin machine move showed a different order of structural transitions than suspected from structural similarities. The immaterial essence or animating principle of integrins revealed here might be said to provide a view into the soul of the integrin machine.

Limitations of the study

The cellular toxicity of reagents that promote photostability of fluorescent dyes used in single-molecule FRET hinders experiments similar to those here with living cells. In our system, we measured only the effect of talin, which regulates the equilibria between the BC, EC, and EO states. Kindlin binds to the C-terminal part of the β-cytoplasmic domain distal from the α-cytoplasmic domain and is not expected to regulate the equilibria between different integrin conformational states. Kindlin and other adaptors may collaborate[69–72] in association of integrins with the actin cytoskeleton and their contribution to single-molecule dynamics remains to be investigated. The conformational transitions reported here are measured in the absence of force. Future technical advances and validation with fiducial markers are needed to determine single integrin conformational transition rates in the presence of force.

STAR★METHODS

Detailed methods are provided in the online version of this paper and include the following:

SUPPLEMENTAL INFORMATION

Supplemental information can be found online at https://doi.org/10.1016/j.cell.2024.04.049.

ACKNOWLEDGMENTS

This work was supported by NIH grant R01-HL-131729, National Science Foundation grants PHY1430124 and EF1934864, and a Boston Children's Hospital Faculty Career Development Fellowship. T. Ha is an investigator of the Howard Hughes Medical Institute.

We thank Dr. Edward A. Lemke for providing the pyrrolysine tRNA synthetase and tRNA plasmid, Dr. Jason W. Chin for the eRF1E55D plasmid, Dr. James Munro for helpful discussions on the amber suppression system, and Dr. Mark H. Ginsberg for CHO αIIbβ3 cell line. We thank Margaret Nielsen for helping with figure preparation.

AUTHOR CONTRIBUTIONS

J. Li designed experiments, labeled protein, and analyzed data; M.H.J. did single-molecule FRET measurements and supervised data analysis; J.Y. did clone work and purified protein; T. Hall did clone work; J. Lee and U.L.-S. did the work on purified α4β1 full-length; S.Y. updated the HaMMy Software and helped with data analysis; T. Ha and T.A.S. supervised research; and J. Li, T. Ha, and T.A.S. wrote the paper with contributions from M.H.J. T.A.S. designed experiments and provided structural interpretations and modeled an integrin intermediate conformational state.

DECLARATION OF INTERESTS

The authors declare no competing financial interests.

Received: October 27, 2023
Revised: February 21, 2024
Accepted: April 30, 2024
Published: May 30, 2024

REFERENCES

1. Hynes, R.O., Ruoslahti, E., and Springer, T.A. (2022). Reflections on integrins–Past, present, and future: The Albert Lasker Basic Medical Research Award. JAMA *328*, 1291–1292. https://doi.org/10.1001/jama.2022.17005.
2. Takagi, J., Petre, B.M., Walz, T., and Springer, T.A. (2002). Global conformational rearrangements in integrin extracellular domains in outside-in and inside-out signaling. Cell *110*, 599–611. https://doi.org/10.1016/s0092-8674(02)00935-2.

3. Li, J., Su, Y., Xia, W., Qin, Y., Humphries, M.J., Vestweber, D., Cabañas, C., Lu, C., and Springer, T.A. (2017). Conformational equilibria and intrinsic affinities define integrin activation. EMBO J. *36*, 629–645. https://doi.org/10.15252/embj.201695803.

4. Li, J., and Springer, T.A. (2018). Energy landscape differences among integrins establish the framework for understanding activation. J. Cell Biol. *217*, 397–412. https://doi.org/10.1083/jcb.201701169.

5. Tadokoro, S., Shattil, S.J., Eto, K., Tai, V., Liddington, R.C., de Pereda, J.M., Ginsberg, M.H., and Calderwood, D.A. (2003). Talin binding to integrin β tails: a final common step in integrin activation. Science *302*, 103–106. https://doi.org/10.1126/science.1086652.

6. Sun, Z., Costell, M., and Fässler, R. (2019). Integrin activation by talin, kindlin and mechanical forces. Nat. Cell Biol. *21*, 25–31. https://doi.org/10.1038/s41556-018-0234-9.

7. Vicente-Manzanares, M., Choi, C.K., and Horwitz, A.R. (2009). Integrins in cell migration–the actin connection. J. Cell Sci. *122*, 199–206. https://doi.org/10.1242/jcs.018564.

8. Calderwood, D.A., Campbell, I.D., and Critchley, D.R. (2013). Talins and kindlins: partners in integrin-mediated adhesion. Nat. Rev. Mol. Cell Biol. *14*, 503–517. https://doi.org/10.1038/nrm3624.

9. Calderwood, D.A., Zent, R., Grant, R., Rees, D.J., Hynes, R.O., and Ginsberg, M.H. (1999). The talin head domain binds to integrin β subunit cytoplasmic tails and regulates integrin activation. J. Biol. Chem. *274*, 28071–28074.

10. Kechagia, J.Z., Ivaska, J., and Roca-Cusachs, P. (2019). Integrins as biomechanical sensors of the microenvironment. Nat. Rev. Mol. Cell Biol. *20*, 457–473. https://doi.org/10.1038/s41580-019-0134-2.

11. Klapholz, B., and Brown, N.H. (2017). Talin - the master of integrin adhesions. J. Cell Sci. *130*, 2435–2446. https://doi.org/10.1242/jcs.190991.

12. Galbraith, C.G., Yamada, K.M., and Galbraith, J.A. (2007). Polymerizing actin fibers position integrins primed to probe for adhesion sites. Science *315*, 992–995. https://doi.org/10.1126/science.1137904.

13. Kim, C., Ye, F., and Ginsberg, M.H. (2011). Regulation of integrin activation. Annu. Rev. Cell Dev. Biol. *27*, 321–345. https://doi.org/10.1146/annurev-cellbio-100109-104104.

14. Li, J., Yan, J., and Springer, T.A. (2021). Low-affinity integrin states have faster ligand-binding kinetics than the high-affinity state. Elife *10*, e73359. https://doi.org/10.7554/eLife.73359.

15. Dustin, M.L., and Springer, T.A. (1989). T-cell receptor cross-linking transiently stimulates adhesiveness through LFA-1. Nature *341*, 619–624. https://doi.org/10.1038/341619a0.

16. Bazzoni, G., and Hemler, M.E. (1998). Are changes in integrin affinity and conformation overemphasized? Trends Biochem. Sci. *23*, 30–34.

17. Nordenfelt, P., Elliott, H.L., and Springer, T.A. (2016). Coordinated integrin activation by actin-dependent force during T-cell migration. Nat. Commun. *7*, 13119. https://doi.org/10.1038/ncomms13119.

18. Nordenfelt, P., Moore, T.I., Mehta, S.B., Kalappurakkal, J.M., Swaminathan, V., Koga, N., Lambert, T.J., Baker, D., Waters, J.C., Oldenbourg, R., et al. (2017). Direction of actin flow dictates integrin LFA-1 orientation during leukocyte migration. Nat. Commun. *8*, 2047. https://doi.org/10.1038/s41467-017-01848-y.

19. Zhang, Y., Qiu, Y., Blanchard, A.T., Chang, Y., Brockman, J.M., Ma, V.P.Y., Lam, W.A., and Salaita, K. (2018). Platelet integrins exhibit anisotropic mechanosensing and harness piconewton forces to mediate platelet aggregation. Proc. Natl. Acad. Sci. USA *115*, 325–330. https://doi.org/10.1073/pnas.1710828115.

20. Li, J., and Springer, T.A. (2017). Integrin extension enables ultrasensitive regulation by cytoskeletal force. Proc. Natl. Acad. Sci. USA *114*, 4685–4690. https://doi.org/10.1073/pnas.1704171114.

21. Chang, A.C., Mekhdjian, A.H., Morimatsu, M., Denisin, A.K., Pruitt, B.L., and Dunn, A.R. (2016). Single molecule force measurements in living cells reveal a minimally tensioned integrin state. ACS Nano *10*, 10745–10752. https://doi.org/10.1021/acsnano.6b03314.

22. Wang, X., and Ha, T. (2013). Defining single molecular forces required to activate integrin and notch signaling. Science *340*, 991–994. https://doi.org/10.1126/science.1231041.

23. Jo, M.H., Li, J., Jaumouillé, V., Hao, Y., Coppola, J., Yan, J., Waterman, C.M., Springer, T.A., and Ha, T. (2022). Single-molecule characterization of subtype-specific β1 integrin mechanics. Nat. Commun. *13*, 7471. https://doi.org/10.1038/s41467-022-35173-w.

24. Roy, R., Hohng, S., and Ha, T. (2008). A practical guide to single-molecule FRET. Nat. Methods *5*, 507–516. https://doi.org/10.1038/nmeth.1208.

25. Ha, T., Enderle, T., Ogletree, D.F., Chemla, D.S., Selvin, P.R., and Weiss, S. (1996). Probing the interaction between two single molecules: fluorescence resonance energy transfer between a single donor and a single acceptor. Proc. Natl. Acad. Sci. USA *93*, 6264–6268. https://doi.org/10.1073/pnas.93.13.6264.

26. Munro, J.B., Gorman, J., Ma, X., Zhou, Z., Arthos, J., Burton, D.R., Koff, W.C., Courter, J.R., Smith, A.B., 3rd, Kwong, P.D., et al. (2014). Conformational dynamics of single HIV-1 envelope trimers on the surface of native virions. Science *346*, 759–763. https://doi.org/10.1126/science.1254426.

27. Asher, W.B., Terry, D.S., Gregorio, G.G.A., Kahsai, A.W., Borgia, A., Xie, B., Modak, A., Zhu, Y., Jang, W., Govindaraju, A., et al. (2022). GPCR-mediated β-arrestin activation deconvoluted with single-molecule precision. Cell *185*, 1661–1675.e16. https://doi.org/10.1016/j.cell.2022.03.042.

28. Liauw, B.W.H., Afsari, H.S., and Vafabakhsh, R. (2021). Conformational rearrangement during activation of a metabotropic glutamate receptor. Nat. Chem. Biol. *17*, 291–297. https://doi.org/10.1038/s41589-020-00702-5.

29. Zhao, Y., Terry, D.S., Shi, L., Quick, M., Weinstein, H., Blanchard, S.C., and Javitch, J.A. (2011). Substrate-modulated gating dynamics in a Na+-coupled neurotransmitter transporter homologue. Nature *474*, 109–113. https://doi.org/10.1038/nature09971.

30. Dolino, D.M., Chatterjee, S., MacLean, D.M., Flatebo, C., Bishop, L.D.C., Shaikh, S.A., Landes, C.F., and Jayaraman, V. (2017). The structure-energy landscape of NMDA receptor gating. Nat. Chem. Biol. *13*, 1232–1238. https://doi.org/10.1038/nchembio.2487.

31. Lu, M., Ma, X., Castillo-Menendez, L.R., Gorman, J., Alsahafi, N., Ermel, U., Terry, D.S., Chambers, M., Peng, D., Zhang, B., et al. (2019). Associating HIV-1 envelope glycoprotein structures with states on the virus observed by smFRET. Nature *568*, 415–419. https://doi.org/10.1038/s41586-019-1101-y.

32. Ley, K., Rivera-Nieves, J., Sandborn, W.J., and Shattil, S. (2016). Integrin-based therapeutics: biological basis, clinical use and new drugs. Nat. Rev. Drug Discov. *15*, 173–183. https://doi.org/10.1038/nrd.2015.10.

33. Lin, F.Y., Li, J., Xie, Y., Zhu, J., Huong Nguyen, T.T., Zhang, Y., Zhu, J., and Springer, T.A. (2022). A general chemical principle for creating closure-stabilizing integrin inhibitors. Cell *185*, 3533–3550.e27. https://doi.org/10.1016/j.cell.2022.08.008.

34. Nikic, I., Estrada Girona, G., Kang, J.H., Paci, G., Mikhaleva, S., Koehler, C., Shymanska, N.V., Ventura Santos, C., Spitz, D., and Lemke, E.A. (2016). Debugging eukaryotic genetic code expansion for site-specific Click-PAINT super-resolution microscopy. Angew Chem. Int. Ed. Engl. *55*, 16172–16176. https://doi.org/10.1002/anie.201608284.

35. Schmied, W.H., Elsässer, S.J., Uttamapinant, C., and Chin, J.W. (2014). Efficient multisite unnatural amino acid incorporation in mammalian cells via optimized pyrrolysyl tRNA synthetase/tRNA expression and engineered eRF1. J. Am. Chem. Soc. *136*, 15577–15583. https://doi.org/10.1021/ja5069728.

36. Beliu, G., Kurz, A.J., Kuhlemann, A.C., Behringer-Pliess, L., Meub, M., Wolf, N., Seibel, J., Shi, Z.D., Schnermann, M., Grimm, J.B., et al. (2019). Bioorthogonal labeling with tetrazine-dyes for super-resolution microscopy. Commun. Biol. *2*, 261. https://doi.org/10.1038/s42003-019-0518-z.

37. Lang, K., and Chin, J.W. (2014). Bioorthogonal reactions for labeling proteins. ACS Chem. Biol. *9*, 16–20. https://doi.org/10.1021/cb4009292.

38. McKinney, S.A., Joo, C., and Ha, T. (2006). Analysis of single-molecule FRET trajectories using hidden Markov modeling. Biophys. J. *91*, 1941–1951. https://doi.org/10.1529/biophysj.106.082487.

39. Thompson, A.A., Liu, J.J., Chun, E., Wacker, D., Wu, H., Cherezov, V., and Stevens, R.C. (2011). GPCR stabilization using the bicelle-like architecture of mixed sterol-detergent micelles. Methods *55*, 310–317. https://doi.org/10.1016/j.ymeth.2011.10.011.

40. Liang, Y.L., Khoshouei, M., Radjainia, M., Zhang, Y., Glukhova, A., Tarrasch, J., Thal, D.M., Furness, S.G.B., Christopoulos, G., Coudrat, T., et al. (2017). Phase-plate cryo-EM structure of a class B GPCR-G-protein complex. Nature *546*, 118–123. https://doi.org/10.1038/nature22327.

41. Zhao, J., Lin King, J.V., Paulsen, C.E., Cheng, Y., and Julius, D. (2020). Irritant-evoked activation and calcium modulation of the TRPA1 receptor. Nature *585*, 141–145. https://doi.org/10.1038/s41586-020-2480-9.

42. Zhang, P., Azizi, L., Kukkurainen, S., Gao, T., Baikoghli, M., Jacquier, M.C., Sun, Y., Määttä, J.A.E., Cheng, R.H., Wehrle-Haller, B., et al. (2020). Crystal structure of the FERM-folded talin head reveals the determinants for integrin binding. Proc. Natl. Acad. Sci. USA *117*, 32402–32412. https://doi.org/10.1073/pnas.2014583117.

43. Chinthalapudi, K., Rangarajan, E.S., and Izard, T. (2018). The interaction of talin with the cell membrane is essential for integrin activation and focal adhesion formation. Proc. Natl. Acad. Sci. USA *115*, 10339–10344. https://doi.org/10.1073/pnas.1806275115.

44. Moser, M., Legate, K.R., Zent, R., and Fässler, R. (2009). The tail of integrins, talin and kindlins. Science *324*, 895–899.

45. Ye, F., Hu, G., Taylor, D., Ratnikov, B., Bobkov, A.A., McLean, M.A., Sligar, S.G., Taylor, K.A., and Ginsberg, M.H. (2010). Recreation of the terminal events in physiological integrin activation. J. Cell Biol. *188*, 157–173. https://doi.org/10.1083/jcb.200908045.

46. Lin, K.c., Ateeq, H.S., Hsiung, S.H., Chong, L.T., Zimmerman, C.N., Castro, A., Lee, W.C., Hammond, C.E., Kalkunte, S., Chen, L.L., et al. (1999). Selective, tight-binding inhibitors of integrin $\alpha_4\beta_1$ that inhibit allergic airway responses. J. Med. Chem. *42*, 920–934.

47. Kim, C., Ye, F., Hu, X., and Ginsberg, M.H. (2012). Talin activates integrins by altering the topology of the beta transmembrane domain. J. Cell Biol. *197*, 605–611. https://doi.org/10.1083/jcb.201112141.

48. Shattil, S.J., Hoxie, J.A., Cunningham, M., and Brass, L.F. (1985). Changes in the platelet membrane glycoprotein IIb.IIIa complex during platelet activation. J. Biol. Chem. *260*, 11107–11114.

49. Schumacher, S., Dedden, D., Nunez, R.V., Matoba, K., Takagi, J., Biertümpfel, C., and Mizuno, N. (2021). Structural insights into integrin $\alpha5\beta1$ opening by fibronectin ligand. Sci. Adv. *7*, eabe9716. https://doi.org/10.1126/sciadv.abe9716.

50. Springer, T.A., and Dustin, M.L. (2012). Integrin inside-out signaling and the immunological synapse. Curr. Opin. Cell Biol. *24*, 107–115. https://doi.org/10.1016/j.ceb.2011.10.004.

51. Kanchanawong, P., and Calderwood, D.A. (2023). Organization, dynamics and mechanoregulation of integrin-mediated cell-ECM adhesions. Nat. Rev. Mol. Cell Biol. *24*, 142–161. https://doi.org/10.1038/s41580-022-00531-5.

52. Shapiro, L., Fannon, A.M., Kwong, P.D., Thompson, A., Lehmann, M.S., Grübel, G., Legrand, J.-F., Als-Nielsen, J., Colman, D.R., and Hendrickson, W.A. (1995). Structural basis of cell-cell adhesion by cadherins. Nature *374*, 327–337.

53. Kim, M., Carman, C.V., Yang, W., Salas, A., and Springer, T.A. (2004). The primacy of affinity over clustering in regulation of adhesiveness of the integrin $\alpha_L\beta_2$. J. Cell Biol. *167*, 1241–1253.

54. Wegener, K.L., Partridge, A.W., Han, J., Pickford, A.R., Liddington, R.C., Ginsberg, M.H., and Campbell, I.D. (2007). Structural basis of integrin activation by talin. Cell *128*, 171–182.

55. Su, Y., Xia, W., Li, J., Walz, T., Humphries, M.J., Vestweber, D., Cabañas, C., Lu, C., and Springer, T.A. (2016). Relating conformation to function in integrin $\alpha5\beta1$. Proc. Natl. Acad. Sci. USA *113*, E3872–E3881. https://doi.org/10.1073/pnas.1605074113.

56. Klapproth, S., Moretti, F.A., Zeiler, M., Ruppert, R., Breithaupt, U., Mueller, S., Haas, R., Mann, M., Sperandio, M., Fässler, R., and Moser, M. (2015). Minimal amounts of kindlin-3 suffice for basal platelet and leukocyte functions in mice. Blood *126*, 2592–2600. https://doi.org/10.1182/blood-2015-04-639310.

57. Jo, M.H., Meneses, P., Yang, O., Carcamo, C.C., Pangeni, S., and Ha, T.J. (2024). Determination of single molecule loading rate during mechanotransduction. Science *383*, 1374–1379.

58. Bachir, A.I., Zareno, J., Moissoglu, K., Plow, E.F., Gratton, E., and Horwitz, A.R. (2014). Integrin-associated complexes form hierarchically with variable stoichiometry in nascent adhesions. Curr. Biol. *24*, 1845–1853. https://doi.org/10.1016/j.cub.2014.07.011.

59. Horrigan, F.T., Cui, J., and Aldrich, R.W. (1999). Allosteric voltage gating of potassium channels I. Mslo ionic currents in the absence of Ca(2+). J. Gen. Physiol. *114*, 277–304.

60. Grosman, C., and Auerbach, A. (2000). Kinetic, mechanistic, and structural aspects of unliganded gating of acetylcholine receptor channels: a single-channel study of second transmembrane segment 12' mutants. J. Gen. Physiol. *115*, 621–635.

61. Wang, S., Vafabakhsh, R., Borschel, W.F., Ha, T., and Nichols, C.G. (2016). Structural dynamics of potassium-channel gating revealed by single-molecule FRET. Nat. Struct. Mol. Biol. *23*, 31–36. https://doi.org/10.1038/nsmb.3138.

62. Manglik, A., Kim, T.H., Masureel, M., Altenbach, C., Yang, Z., Hilger, D., Lerch, M.T., Kobilka, T.S., Thian, F.S., Hubbell, W.L., et al. (2015). Structural Insights into the Dynamic Process of β2-Adrenergic Receptor Signaling. Cell *161*, 1101–1111. https://doi.org/10.1016/j.cell.2015.04.043.

63. Vilardaga, J.P., Bünemann, M., Krasel, C., Castro, M., and Lohse, M.J. (2003). Measurement of the millisecond activation switch of G protein-coupled receptors in living cells. Nat. Biotechnol. *21*, 807–812.

64. Zhao, Y., Terry, D., Shi, L., Weinstein, H., Blanchard, S.C., and Javitch, J.A. (2010). Single-molecule dynamics of gating in a neurotransmitter transporter homologue. Nature *465*, 188–193. https://doi.org/10.1038/nature09057.

65. Xie, C., Zhu, J., Chen, X., Mi, L., Nishida, N., and Springer, T.A. (2010). Structure of an integrin with an αI domain, complement receptor type 4. EMBO J. *29*, 666–679. https://doi.org/10.1038/emboj.2009.367.

66. Goldsmith, J.A., DiVenere, A.M., Maynard, J.A., and McLellan, J.S. (2022). Structural basis for non-canonical integrin engagement by Bordetella adenylate cyclase toxin. Cell Rep. *40*, 111196. https://doi.org/10.1016/j.celrep.2022.111196.

67. Zhu, J., Luo, B.H., Xiao, T., Zhang, C., Nishida, N., and Springer, T.A. (2008). Structure of a complete integrin ectodomain in a physiologic resting state and activation and deactivation by applied forces. Mol. Cell *32*, 849–861. https://doi.org/10.1016/j.molcel.2008.11.018.

68. Dong, X., Mi, L.Z., Zhu, J., Wang, W., Hu, P., Luo, B.H., and Springer, T.A. (2012). αVβ3 integrin crystal structures and their functional implications. Biochemistry *51*, 8814–8828.

69. Theodosiou, M., Widmaier, M., Böttcher, R.T., Rognoni, E., Veelders, M., Bharadwaj, M., Lambacher, A., Austen, K., Müller, D.J., Zent, R., and Fässler, R. (2016). Kindlin-2 cooperates with talin to activate integrins and induces cell spreading by directly binding paxillin. Elife *5*, e10130. https://doi.org/10.7554/eLife.10130.

70. Bodescu, M.A., Aretz, J., Grison, M., Rief, M., and Fässler, R. (2023). Kindlin stabilizes the talin.integrin bond under mechanical load by generating an ideal bond. Proc. Natl. Acad. Sci. USA *120*, e2218116120. https://doi.org/10.1073/pnas.2218116120.

71. Aretz, J., Aziz, M., Strohmeyer, N., Sattler, M., and Fässler, R. (2023). Talin and kindlin use integrin tail allostery and direct binding to activate

integrins. Nat. Struct. Mol. Biol. *30*, 1913–1924. https://doi.org/10.1038/s41594-023-01139-9.

72. Fischer, L.S., Klingner, C., Schlichthaerle, T., Strauss, M.T., Böttcher, R., Fässler, R., Jungmann, R., and Grashoff, C. (2021). Quantitative single-protein imaging reveals molecular complex formation of integrin, talin, and kindlin during cell adhesion. Nat. Commun. *12*, 919. https://doi.org/10.1038/s41467-021-21142-2.
73. Mould, A.P., Garratt, A.N., Askari, J.A., Akiyama, S.K., and Humphries, M.J. (1995). Identification of a novel anti-integrin monoclonal antibody that recognises a ligand-induced binding site epitope on the β1 subunit. FEBS Lett. *363*, 118–122. https://doi.org/10.1016/0014-5793(95)00301-o.
74. Mould, A.P., Travis, M.A., Barton, S.J., Hamilton, J.A., Askari, J.A., Craig, S.E., Macdonald, P.R., Kammerer, R.A., Buckley, P.A., and Humphries, M.J. (2005). Evidence that monoclonal antibodies directed against the integrin β subunit plexin/semaphorin/integrin domain stimulate function by inducing receptor extension. J. Biol. Chem. *280*, 4238–4246.
75. Lenter, M., Uhlig, H., Hamann, A., Jenö, P., Imhof, B., and Vestweber, D. (1993). A monoclonal antibody against an activation epitope on mouse integrin chain β1 blocks adhesion of lymphocytes to the endothelial integrin α6β1. Proc. Natl. Acad. Sci. USA *90*, 9051–9055. https://doi.org/10.1073/pnas.90.19.9051.
76. Akiyama, S.K., Yamada, S.S., Chen, W.T., and Yamada, K.M. (1989). Analysis of fibronectin receptor function with monoclonal antibodies: Roles in cell adhesion, migration, matrix assembly, and cytoskeletal organization. J. Cell Biol. *109*, 863–875. https://doi.org/10.1083/jcb.109.2.863.
77. Miyake, K., Hasunuma, Y., Yagita, H., and Kimoto, M. (1992). Requirement for VLA-4 and VLA-5 integrins in lymphoma cells binding to and migration beneath stromal cells in culture. J. Cell Biol. *119*, 653–662. https://doi.org/10.1083/jcb.119.3.653.
78. Frelinger, A.L., 3rd, Du, X.P., Plow, E.F., and Ginsberg, M.H. (1991). Monoclocal antibodies to ligand-occupied conformers of integrin αIIbβ3 (glycoprotein IIb-IIIa) alter receptor affinity, specificity, and function. J. Biol Chem *266*, 17106–17111.
79. Liu, X., Zhang, Y., Chen, Y., Li, M., Zhou, F., Li, K., Cao, H., Ni, M., Liu, Y., Gu, Z., et al. (2017). In Situ Capture of Chromatin Interactions by Biotinylated dCas9. Cell *170*, 1028–1043.e19. https://doi.org/10.1016/j.cell.2017.08.003.
80. Ran, F.A., Hsu, P.D., Wright, J., Agarwala, V., Scott, D.A., and Zhang, F. (2013). Genome engineering using the CRISPR-Cas9 system. Nat. Protoc. *8*, 2281–2308. https://doi.org/10.1038/nprot.2013.143.
81. Nikic, I., Kang, J.H., Girona, G.E., Aramburu, I.V., and Lemke, E.A. (2015). Labeling proteins on live mammalian cells using click chemistry. Nat. Protoc. *10*, 780–791. https://doi.org/10.1038/nprot.2015.045.
82. Wysocki, L.J., and Sato, V.L. (1978). "Panning" for lymphocytes: A method for cell selection. Proc. Natl. Acad. Sci. USA *75*, 2844–2848.
83. Zhang, C., Liu, J., Jiang, X., Haydar, N., Zhang, C., Shan, H., and Zhu, J. (2013). Modulation of integrin activation and signaling by α1/α1'-helix unbending at the junction. J. Cell Sci. *126*, 5735–5747. https://doi.org/10.1242/jcs.137828.
84. Clark, K., Pankov, R., Travis, M.A., Askari, J.A., Mould, A.P., Craig, S.E., Newham, P., Yamada, K.M., and Humphries, M.J. (2005). A specific α5β1-integrin conformation promotes directional integrin translocation and fibronectin matrix formation. J. Cell Sci. *118*, 291–300. https://doi.org/10.1242/jcs.01623.
85. Takagi, J., Erickson, H.P., and Springer, T.A. (2001). C-terminal opening mimics "inside-out" activation of integrin α5β1. Nat. Struct. Biol. *8*, 412–416.

STAR★METHODS

KEY RESOURCES TABLE

REAGENT or RESOURCE	SOURCE	IDENTIFIER
Antibodies		
12G10	Hybridoma from Martin Humphries[73]	N/A
8E3	Hybridoma from Martin J. Humphries[74]	N/A
9EG7	Hybridoma from Dietmar Vestweber[75]	N/A
mAb13	Hybridoma from Kenneth Yamada[76]	N/A
MBC319.4	Hybridoma from Richard Aster (Versiti Blood Research Institute and Medical College of Wisconsin)	N/A
SG19	Hybridoma from Jun Takagi[77]	N/A
SNAKA51	Hybridoma from Martin J. Humphries[74]	N/A
LIBS6	Hybridoma from Mark Ginsberg[78]	N/A
mAb16	Hybridoma from Kenneth Yamada[76]	N/A
PAC-1	BioLegend	Cat# 362802; RRID:AB_2563889
Anti-IgM	BioLegend	Cat# 406509; RRID:AB_315059
Chemicals, peptides, and recombinant proteins		
08:0 PI(4,5)P2	Avanti Polar Lipids	Cat# 850185
08:0 PI(3,4,5)P3	Avanti Polar Lipids	Cat# 850186
ACRGDGWCG peptide	Li et al.[3] – custom synthesis by GenScript	N/A
Bovine serum albumin	Thermo Scientific	Cat# 37525
Catalase	Sigma-Aldrich	Cat# C30
D(+)-Biotin	Sigma	Cat# 8512090005
D(+)-Glucose	Sigma	Cat# G8769-100ML
Desthiobiotin	Neuromics	Cat# 2-1000-002
Dodecylmaltoside/CHS	Anatrace	Cat# D310-CH210
Eptifibatide	Sigma-Aldrich	CAS# 188627-80-7
Expi293 Expression Medium	Life Tech	Cat# A1435102
FectoPRO	Polyplus	Cat# 101000007
FITC-Ahx-ACRGDGWCG peptide	Li et al.[3] – custom synthesis by GenScript	N/A
Freestyle 293 Expression Medium	Life Tech	Cat# 12338026
Glucose oxidase	Sigma-Aldrich	Cat# G2133
JetPrime	Polyplus	Cat# 101000046
Leibovitz's L-15 Medium, no phenol red	Thermofisher	Cat# 21083027
LMNG/CHS	Anatrace	Cat# NG310-CH210
MPEG-SVA-5000	Laysan Bio	Cat# PEG-SVA-5000
MUPA-LDVPAAK peptide	TOCRIS	Catalog # 7020
MUPA-LDVPAAK-FITC	TOCRIS	Catalog # 4577
Neutravidin	Thermo Fisher Scientific	Cat# 31000
PEG-SVA-5000	Laysan Bio	Cat# MPEG-SVA-5000
Opti-MEM	Life Tech	Cat# 31985-070
Protocatechuic acid	Sigma-Aldrich	Cat# 37580
Protocatechuate 3,4-Dioxygenase	OYC Americas	Cat# 46852004
Sodium Valproic Acid	Sigma	Cat# P4543-100G
Sulfo-Cy5-tetrazine	Jena Bioscience	Cat# CLK-015-05

(*Continued on next page*)

Continued

REAGENT or RESOURCE	SOURCE	IDENTIFIER
Sulfo-Cy3-tetrazine	Jena Bioscience	Cat# CLK-014-05
Trans-cyclooct-2-ene ncAA (TCO*)	SiChem	Cat# SC-8008
Trolox	Sigma-Aldrich	Cat# 238813
Experimental models: Cell lines		
CHO αIIbβ3	Cell line provided by Ginsberg Lab[47]	N/A
Expi293F	Thermo Fisher Scientific	Cat# A14527
Expi293F α5&αV knockout cells	Lin et al.[33]	N/A
Expi293F β1 knockout cells	This paper	N/A
E. coli BL21(DE3)	Thermo Fisher Scientific	CAT# EC0114
Recombinant DNA		
Plasmid encoding NESPylRS^{AF}/tRNA^{Pyl}	Plasmid provided by Dr. Edward A. Lemke[34]	N/A
Plasmid encoding eukaryotic release factor 1 mutant: pcDNA5-eRF1-E55D	Plasmid provided by Dr. Jason W. Chin[35]	N/A
Plasmid encoding a BirA enzyme: pEF1a-BirA-V5-neo	Liu et al.[79]	Addgene #100548
Plasmid encoding human integrin α5 ectodomain: PD2529 human α5 ecto	This paper	N/A
Plasmid encoding human integrin α5 full length: PD2529 human α5 full	This paper	N/A
Plasmid encoding human integrin α5 full length: pcDNA3.4 human α5 full	This paper	N/A
Plasmid encoding human integrin α4 full length: pcDNA3.4 human α4 full	This paper	N/A
Plasmid encoding human integrin β1 ectodomain: PD2529 human β1 ecto	This paper	N/A
Plasmid encoding human integrin β1 Q280*K418* ectodomain	This paper	N/A
Plasmid encoding human integrin β1 N391*N562* ectodomain	This paper	N/A
Plasmid encoding human integrin β1 full-length: PD2529 human β1 full	This paper	N/A
Plasmid encoding human integrin β1 Q280* full-length	This paper	N/A
Plasmid encoding human integrin β1 K418* full-length	This paper	N/A
Plasmid encoding human integrin β1 N391* full-length	This paper	N/A
Plasmid encoding human integrin β1 N562* full-length	This paper	N/A
Plasmid encoding human integrin β1 Q280*K418* full-length	This paper	N/A
Plasmid encoding human integrin β1 N391*N562* full-length	This paper	N/A
Plasmid encoding Talin1 head for E.coli expression	Liu et al.[42]	Addgene #166127
Plasmid encoding Talin1 head EGFP fusion for mammalian expression	This paper	N/A
pSpCas9n(BB)-2A-puro	Ran et al.[80]	Addgene #4814

(*Continued on next page*)

Continued

REAGENT or RESOURCE	SOURCE	IDENTIFIER
Software and algorithms		
HaMMy5 – Rewrite of HaMMy4 in Python compatible with MacOS and Windows 10	This paper https://zenodo.org/records/10961125	https://github.com/codergirl1106/HaMMy5
MATLAB	Mathworks	https://www.mathworks.com/products/matlab.html
Mathematica	Wolfram	https://www.wolfram.com/mathematica/
Prism10	GraphPad	https://www.graphpad.com/scientific-software/prism/
PyMOL	Schrödinger Inc.	https://pymol.org/2/
TDP	McKinney et al.[38]	https://github.com/Ha-SingleMoleculeLab/HaMMy

RESOURCE AVAILABILITY

Lead contact

Further information and requests for resources and reagents should be directed to and will be fulfilled by the lead contact, Timothy Springer (springer@crystal.harvard.edu).

QA Materials availability

Plasmids and cell lines generated in the study are available from the lead contact without restriction.

The following plasmids have also been deposited at Addgene:

- Plasmid encoding human integrin α5 ectodomain: PD2529 human α5 ecto
- Plasmid encoding human integrin α5 full length: PD2529 human α5 full
- Plasmid encoding human integrin α5 full length: pcDNA3.4 human α5 full
- Plasmid encoding human integrin α4 full length: pcDNA3.4 human α4 full
- Plasmid encoding human integrin β1 ectodomain: PD2529 human β1 ecto
- Plasmid encoding human integrin β1 Q280*K418* ectodomain
- Plasmid encoding human integrin β1 N391*N562* ectodomain
- Plasmid encoding human integrin β1 full-length: PD2529 human β1 full
- Plasmid encoding human integrin β1 Q280* full-length
- Plasmid encoding human integrin β1 K418* full-length
- Plasmid encoding human integrin β1 N391* full-length
- Plasmid encoding human integrin β1 N562* full-length
- Plasmid encoding human integrin β1 Q280*K418* full-length
- Plasmid encoding human integrin β1 N391*N562* full-length
- Plasmid encoding Talin1 head EGFP fusion for mammalian expression

Data and code availability

- All original single molecule traces and HaMMy5 results have been deposited at Harvard Dataverse: https://doi.org/10.7910/DVN/POVP0W
- Python code for HaMMy5 is available on GitHub (https://github.com/codergirl1106/HaMMy5) and Zenodo (https://zenodo.org/records/10961125).
- Any additional information required to reanalyze the data reported in this paper is available from the lead contact upon request.

EXPERIMENTAL MODEL AND STUDY PARTICIPANT DETAILS

Expi293F, Expi293F α5&αV knockout cells, and Expi293F β1 knockout cells are used for integrin protein production. Expi293F are human embryonic kidney cells sourced from Thermo Fisher (Cat# A14527). Culture conditions and transfection protocol are in method details. Expi293F α5&αV and Expi293F β1 knockout cells were developed from Expi293F in our lab.

All mammalian cell lines in our lab, including hybridomas used for antibody production, are tested for mycoplasma every 60 days and were not authenticated.

E. coli cells, BL21(DE3), are commercially available and were used for expressing fibronectin fragment and talin 1 head. Cells are cultured in lysogeny broth (LB) medium.

METHOD DETAILS

Producing integrin α5β1 FRET reporters

Using an optimized pyrrolysine-based genetic code expansion system,[34,81] we further optimized ratios of transfected plasmids to introduce a click chemistry-compatible lysine derivative, *trans*-cyclooct-2-en-L-lysine (TCO*-Lys), at specific amber (TAG) sites in the β1 subunit for FRET-pair labeling. Integrin α5β1 ectodomain and full-length protein with indicated amber mutations were produced by co-transfecting α5 and β1 cDNAs with C-terminal coiled-coils[2] into Expi293F cells and Expi293F α5& αV knockout cells,[33] respectively. The construct for the α5 ectodomain (codon optimized by ATUM for human mature residues α5 F1 to Y954) in PD2529 CAG vector (ATUM) contains an N-terminal CD33 secretion peptide (MPLLLLLPLLWAGALA) and C-terminal HRV3C cleavage site (LEVLFQG), acid coil (AQCEKELQALEKENAQLEWELQALEKELAQ), Protein C tag (EDQVDPRLIDGK), and Strep twin tag (SAWSHPQFEKGGGSGGGGGSAWSHPQFEK). Construct for the integrin β1 ectodomain amber mutant (codon optimized by ATUM for human mature β1 residues Q1 to D708) in PD2529 CAG vector contains an N-terminal CD33 secretion peptide and C-terminal AVI tag (GLNDIFEAQKIEWHE), HRV3C cleavage site, basic coil (AQCKKKLQALKKKNAQLKWKLQALKKKLAQ), HA tag (YPYDVPDYA) and deca-histidine tag. Human full-length integrin α5 contains the native mature cDNA sequence in PD2529 CAG vector with an N-terminal CD33 secretion peptide. Human full-length integrin β1 contains a codon-optimized mature sequence with an N-terminal CD33 secretion peptide and C-terminal AVI and HA tags.

For TCO*-Lys incorporation, integrin subunits were co-transfected using FectoPRO (Polyplus, #101000014) with the plasmid (pCMV-NES-PylRS (AF) hU6tRMNAPyl) coding for both pyrrolysine tRNA and a mutated pyrrolysine tRNA synthase that accepts the larger TCO*-Lys residue[34] and plasmid (pcDNA5-eRF1-E55D) coding a eukaryotic release factor 1 mutant that decreases polypeptide termination.[35] Additionally, for full-length integrin α5β1 amber mutants, pEF1a-BirA-V5-neo (Addgene Plasmid #100548) was included for *in vivo* biotinylation of the AVI tag.[79] Plasmid ratios were optimized (Figure S1A) and final ratios are shown (Figures S1A and S2C). For every mL of Expi293 cells, 0.8 μg total plasmid and 0.8 μL FectoPro were used. Transfectants were cultured in FreeStyle 293 medium supplemented with 200 μM TCO*-Lys (SiChem GmbH, SC-8008), and for full-length transfectants, with 10 μM biotin. Richer Expi293 medium substantially lowered fluorophore incorporation, likely because of reaction of medium components with TCO*-Lys. Valproic acid and glucose were added to cultures 24 h after transfection to final concentrations of 3 mM and 0.4%, respectively.

After 4 days, integrin α5β1 ectodomain mutants were purified using Ni affinity chromatography, followed by HRV3C cleavage and Superdex 200 chromatography, stochastically labeled with sulfo-Cy3-tetrazine (Jena Bioscience, CLK-014-05) and sulfo-Cy5-tetrazine (Jena Bioscience, CLK-015-05) by click chemistry,[36] and biotinylated with BirA enzyme on the AVI tag at the C termini of the β1 subunit using conditions described in Figure S1A. Protein was further purified with Superdex 200 gel filtration to remove free dyes, biotin and aggregates, flash frozen in one-use aliquots, and stored at −80°C.

After 2 days, sulfo-Cy3-tetrazine and sulfo-Cy5-tetrazine labeling of live cells in Freestyle 293 medium, preparation of lysates in buffer containing 1% LMNG/CHS (10:1, Anatrace, NG310-CH210), and freezing of one-use aliquots at −80°C was as described in Figure S2C.

Expi293F β1 knockout cell line

β1 subunit was knocked out from Expi293F cells using CRISPR double nicking.[80] To make the single-guide RNA (sgRNA) expressing plasmids, double stranded DNA oligos,

5′-CACCG AGTTCTGTTCACTTGTGCAA -3' (β1_guide A top oligo),
5′-AAACTTGCACAAGTGAACAGAACTC -3' (β1_guide A bottom oligo),
5′-CACCGGTGCTCAGTCTTACTAATAA -3' (β1_guide B top oligo),
5′-AAACTTATTAGTAAGACTGAGCACC -3' (β1_guide B bottom oligo),

were cloned into the BbSI site of the pSpCas9n(BB)-2A-puro vector (Addgene Plasmid #48141). To create the Expi293F β1 knockout, the pair of sgRNA expressing plasmids targeting β1 were transfected into Expi293F cells and knock-out cells were selected by two rounds of panning[82] and one round of FACS sorting, both with β1-specific antibody mAb13.[76]

Ligand binding affinity of α5β1 amber mutants

To obtain the high surface expression required for these experiments, Expi293 β1 knockout cells were used at less than 10 passages and all plasmids were from fresh minipreps. As purification was not needed, the biotin ligase was omitted and other plasmids were used at ~10% higher concentrations and biotin was not included in the growth medium. Expi293 β1 knockout cells ($2.5x10^6$/mL in 2 mL) were transfected with 0.2 μg plasmid coding for α5 full-length in PD2529, 0.7 μg plasmid coding for β1 full-length with indicated amber mutations, 0.46 μg plasmid coding for both pyrrolysine tRNA and a mutated pyrrolysine tRNA synthase (pCMV-NES-PylRS (AF) hU6tRMNAPyl), and 0.24 μg plasmid coding a eukaryotic release factor 1 mutant (pcDNA5-eRF1-E55D) with 1.6 μL FectoPRO. Transfectants were cultured in FreeStyle 293 medium supplemented with 200 μM TCO*-Lys. After 24 h 3mM valproic acid and 0.4% glucose were added to the culture. After 48 h, transfectants were washed twice with PBS and resuspended at

6 million/mL in freestyle 293 medium with 4 μM Sulfo-C3 tetrazine for labeling. Labeling was carried out at 37°C for 1 h, followed by two washes in PBS. Washed cells were resuspended in Assay Medium (L15 medium with 1% BSA) for integrin α5β1 expression level check and ligand binding affinity measurements. For α5β1 cell surface expression level check, 100 μL cells contained 2 × 10^6 cells/ml and 10nM Alexa 647-mAb16 antibody in Assay Medium. For ligand binding affinity measurements, each sample (50 μL) contained 2 × 10^6 cells/ml, 1nM Alexa 647-12G10 Fab, and indicated concentrations of cylic-ACRGDGWCG (cRGD) in Assay Medium. The mixture was allowed to equilibrate at 22°C for 1 h before flow cytometry (BD FACSCanto II) without washing.

Purification of wild type full-length α5β1 and α4β1

To make a stable full-length α5β1 cell line, Expi293 cells were co-transfected with wild type human α5 and β1 cDNAs as described for TCO*-Lys incorporation except that α5 in pcDNA3.4 contained a C-terminal Strep twin tag and β1 in PD2529-CAG contained C-terminal HA and AVI tags. Stable transfectants were selected with G418 (500 μg/mL) and puromycin (30 μg/mL) and then further sorted with fluorescently labeled α5β1 mAb16.[76] α5β1 stable transfectants grown in Expi293 medium to ~10 million/mL were collected and washed with PBS. Cell pellets were lysed with Dounce homogenization in 20 mM HEPES buffer (pH 7.4) containing 1 mM Ca^{2+} and 1 mM Mg^{2+} (20 mL lysis buffer for every gram of cells). Cell membranes were collected by ultracentrifugation at 100,000 g and 4°C for 45 min and homogenized in the same volume of membrane solubilization buffer, 20 mM HEPES buffer (pH 7.4) containing 1mM Ca^{2+}, 1mM Mg^{2+}, 150mM NaCl, 5% glycerol and 0.5% dodecylmaltoside/CHS (10:1, Anatrace, D310-CH210). After another ultracentrifugation at 100,000g and 4°C for 1 h, the supernatant was loaded onto a Strep-Tactin Sepharose column for affinity purification. The desthiobiotin eluate was further purified and exchanged into LMNG/CHS using Sepharose 6 Increase size exclusion chromatography in 20mM HEPES, pH 7.4, 1mM Ca^{2+}, 1mM Mg^{2+}, 150mM NaCl, and 0.01% LMNG/CHS and flash frozen at −80°C in one-use aliquots (Figures S2A and S2B). Production and purification of full-length α4β1 followed the same strategy as for full-length α5β1.

Antibodies and preparation of Fabs

Hybridomas were 12G10,[73] 8E3,[74] 9EG7,[75] mAb13 and mAb16,[76] MBC319.4,[83] SG19,[77] SNAKA51,[84] and LIBS6.[78] IgG in hybridoma supernatants was purified with protein G. Fab fragments were prepared with papain digestion at 1 mg/mL IgG and IgG:papain mass ratio of 500:1 in PBS with 10 mM EDTA and 10 mM L-Cysteine at 37°C for 18 h. After buffer exchange with 50 mM Tris-HCl (pH 9), Fabs were purified by anion exchange chromatography (5 mL HiTrap Q HP, GE Healthcare) at 1 mL/min flow rate in Tris-HCl (pH 9) with a gradient in the same buffer to 0.5 M NaCl in 100 min. Fab fractions were concentrated, flash frozen, and stored at −80°C.

Single-molecule fluorescence imaging

Single-molecule fluorescence imaging was performed using a laboratory-built prism type Total Internal Reflection Fluorescence Microscopy (TIRFM) system. The microscopy system was built based on a Nikon Eclipse Ti microscope body, equipped with the Nikon Perfect Focus system. We employed solid-state lasers: a 543 nm laser (Shanghai Dream Lasers Technology) for Cy3, a 637 nm laser (Coherent, OBIS LX) for Cy5, and a 488 nm laser (Coherent, OBIS LS) for Alexa 488. These lasers were combined via a single-mode fiber and directed onto a quartz slide through a prism. Fluorescence signals were collected using a 60X water immersion objective (CFI Plan Apo IR 60XC WI). Emission light was spectrally separated using ultra-flat dichroic mirrors (T540LPXR UF3 for Alexa 488/Cy3 and T635LPXR UF3 for Cy3/Cy5). The scattered laser light was further eliminated by adding a custom notch filter (Chroma, ZET488/543/638/750M) in the optical path. Imaging movies were recorded using an electron-multiplying charge-coupled device (EMCCD; Andor, iXon 897). The system was controlled by laboratory-built software (smCamera2).

All measurements were conducted at room temperature (22°C) unless otherwise specified. For experiments conducted at 37°C, we utilized a custom heating system (Live Cell Instruments, Seoul, Korea). To slow photobleaching of fluorescent probes, oxygen scavenging systems were added to the integrin imaging buffers described below. Glucose oxidase-based buffer containing ~1 mM Trolox (Sigma-Aldrich, 238813), 7.2 g/L dextrose, 0.1 g/L glucose oxidase (Sigma-Aldrich, G2133), and ~0.05 g/L (~500 units/mL) catalase (Sigma-Aldrich, C30) was used for α5β1 ectodomain reporters. Dioxygenase-based buffer containing ~1 mM Trolox, 2.5 mM protocatechuic acid (Sigma-Aldrich, 37580), and 0.2% v/v (~0.01 units/ml) protocatechuate 3,4-Dioxygenase solution (OYC Americas, 46852004) was used for α5β1 full-length reporters.

smFRET measurements and data analysis

For single-molecule imaging using TIRFM, fluorescently labeled and biotinylated integrin constructs were sparsely (0.1–0.2 molecules/μm^2) immobilized on a quartz slide passivated and biotin-functionalized with polyethylene glycol (Laysan Bio, MPEG-SVA-5000 and PEG-SVA-5000).[24] We constructed a flow cell by placing a coverslip and a quartz slide parallel to each other, kept apart by double-sided tape (Scotch, 665). Both the coverslip and slide were PEGylated (Nano Surface Science). The slide features holes to allow buffer flow. To immobilize biotinylated samples, we incubated neutravidin (Thermo Fisher Scientific, 31000; 0.4 mg/mL) within the flow cell for 2 min, followed by incubation with 0.1% w/v bovine serum albumin (BSA; Thermo Scientific, 37525) for further passivation. Phosphate-buffered saline (PBS, pH 7.4) was used as diluent and wash buffer in these steps. Purified α5β1 ectodomain reporters (Figure S1D) or full-length reporters in cell lysate (Figure S2D) were diluted to optimal concentrations (~50 pM) with imaging buffers and incubated for 2–5 min in the flow cell for the sparse immobilization, followed by extensive washing with imaging buffer. Imaging buffer for soluble α5β1 ectodomain reporters contained 20 mM HEPES, pH7.4, 1 mM Ca^{2+}, 1 mM Mg^{2+} and 150 mM NaCl. Imaging buffer for α5β1 full-length reporters (Figures 4 and 5) contained 20 mM HEPES, pH7.4, 1 mM Ca^{2+}, 1 mM Mg^{2+},150 mM NaCl,

and 0.01% LMNG/CHS. For the experiments comparing the presence and absence of talin1 head (Figures 6B–6F), the imaging buffer contained 20 mM HEPES, pH7.4, 0.1 mM Ca^{2+}, 1 mM Mg^{2+}, 50 mM KCl, 0.01% LMNG/CHS, with or without 0.002% 08:0 PI(4,5)P2 (Avanti Polar Lipids, 850185). Imaging buffers supplemented with the oxygen scavenging reagents described above were injected into the flow cell just before measurements. When present, Fab, ligand, or talin1 head were injected together, and incubated with the integrin in the flow cell for 5 min before measurements. To correct background signal in TIRF images, we created a two-dimensional background intensity profile for each color channel (Cy3 and Cy5, 512x256 pixels). We first averaged 10 frames and analyzed the pixel intensity distribution within 16x8 smaller grids (32x32 pixels). Given the low density of single molecules, most pixels contain background signal. Thus, for each grid, we chose the most frequent pixel intensity as the representative background value. Smoothing these representative values across the entire image generated the background intensity profile for each channel. When single-molecule fluorescent spots were found, the background intensity at the spot's location was simply retrieved from the corresponding profile. This procedure was implemented using an Interactive Data Language (IDL) script.

For FRET measurements, the donor (Cy3) of the FRET reporters was excited, and both donor and acceptor (Cy5) signals were recorded. The acceptor was directly excited before and after the FRET measurement (typically 30 s) to check the presence of acceptor. All molecules with the acceptor signal were collected. Single-molecule fluorescence spot detection and their intensity time trace generation were conducted using Interactive Data Language (IDL) scripts.

For 3-color measurements (Alexa 488, Cy3, and Cy5), each dye was sequentially illuminated using a corresponding laser while all three-color channel signals were continuously recorded. The FRET efficiency between Cy3 and Cy5 was calculated using the signals obtained when Cy3 is illuminated.

The intensity time traces were examined using MATLAB (Mathworks) scripts and traces with a donor-acceptor pair were chosen for further analysis. The smFRET trajectories were identified according to the following criteria: (1) donor and acceptor fluorescence trajectories either displayed a single photobleaching event, which is indicative of a single FRETing fluorophore pair per molecule, or continued for the entire 30 s measurement; the donor and acceptor intensities showed anti-correlated changes and the sum of donor and acceptor intensities was characteristic of a single molecule based on the laser power used; (2) FRET was detectable for minimally 15 frames before photobleaching. Corrected fluorescence time traces were used to calculate apparent FRET efficiency according to $FRET = I_A/(\gamma I_D+I_A)$, where I_A and I_D are the fluorescence emission intensities of the acceptor and donor fluorescence, respectively, and γ is the empirically determined ratio of detection efficiencies in the acceptor and donor channels. All smFRET trajectories were fit to a hidden Markov model (HMM) consisting of two states with HaMMy.[38] The previous HaMMy C++ code only runs on out-of-date Windows systems and is falling out of use. Therefore, we rewrote the code and GUI using python to run on multiple platforms; we ran it on a Mac. The new HaMMy5.py code and readme file are deposited at GitHub. HaMMy5 was used to calculate the dwell times of FRET states between transitions and to compile dwell time histograms. The median dwell time in each distribution was used as bin widths. State frequency (F) in each bin at time t was fit to single exponential decay, $F = F_0 \exp\left(-\frac{t}{\tau}\right)$, where F_0 is F at $t = 0$, to determine the lifetime (τ) of the FRET state, and its inverse, the transition rate. The numbers of single molecule traces analyzed under each condition are shown in Table S1.

Dynamic light scattering (DLS)

Data shown in Figure S4A were measured by dynamic light scattering. Each sample (25 μL) in 20mM HEPES, pH 7.4, 1mM Ca^{2+}, 1mM Mg^{2+}, 150mM NaCl, 0.1% LMNG/CHS contained differing experimental concentrations of 08:0 PI(4,5)P2 or 08:0 PI(3,4,5)P3 as w/w % of LMNG/CHS. Solution was placed in a 384 well black clear bottom plate (Aurora Microplates, #ABM2-10100A). Measurements were taken on a DynaPro Plate Reader III (Wyatt Technology) at 0.1 μs intervals at 25°C. Average hydrodynamic radii were calculated using DYNAMICS (Wyatt Technology).

Fluorescence polarization

Each sample (10 μL) in 20 mM HEPES, pH 7.4, 150 mM NaCl, 1 mM Ca^{2+}, 1 mM Mg^{2+} and 0.01% LMNG/CHS contained differing indicated concentrations of PIP2 analog, Fabs, and talin1 head (Figures S5B and 6A) and differing indicated concentrations of FITC-cRGD and purified full-length α5β1 (Figures S5B and 6A). Mixtures were allowed to equilibrate for 2 h (or 24 h with 12G10 Fab) at 22°C before recording FP on a Synergy *NEO* HTS multi-mode microplate reader (Biotek). Affinities of α5β1 for FITC-cRGD were obtained from fits to Equation S16 in the Appendix of Li et al., 2017,[3] which is also shown below:

$$FP_{obs} = FP_L + \frac{[L]+K_d+[\alpha5\beta1]-\sqrt{([L]+K_d+[\alpha5\beta1])^2-4[L][\alpha5\beta1]}}{2[L]}\left(FP_{\alpha5\beta1\bullet L}-FP_L\right)$$

FP_L and $FP_{\alpha5\beta1\cdot L}$ are FP of free and α5β1-bound FITC-cRGD, respectively, [α5β1] is the total concentration of soluble α5β1 in solution, [L] is the total concentration of the ligand FITC-cRGD, and K_d is the binding affinity of α5β1 for FITC-cRGD. Fitting the observed FP value, FP_{obs}, and [α5β1] to the equation yields K_d, FP_L, and $FP_{\alpha5\beta1\cdot L}$.

Preparation of ligand and talin1 head

Human fibronectin fragment $Fn3_{9-10}$ (mature residues G1326 to T1509) and its N terminal cysteine addition mutant were expressed in E. coli BL21(DE3) cells and purified as described.[85] The mutant was fluorescently labeled with Alexa Fluor 488 C5 maleimide

(ThermoFisher Scientific) in PBS. Talin1 head (human talin1 M1 to K405) was expressed using pTrcHis C vector (Addgene Plasmid #166127) and purified from E.coli as described.[42] Purity was assessed by SDS-PAGE (sodium dodecyl sulfate polyacrylamide gel electrophoresis) (Figure S5A). To construct the talin1 head EGFP fusion used for transfection in mammalian cells, codons for talin1, M1 to K405, were amplified from pTrcHis C talin1 head vector and cloned into pEGFP-N1 (Addgene Plasmid #60360). pEGFP-N1-Flag was also used as a control.

Cell surface ligand binding affinity assays

Expi293 α5&αV knockout cells[33] ($5x10^6$ in 2 mL) were transfected with 0.6 μg wild type full length α5 or α4 in plasmid PD2529 and 1 μg talin1 head-EGFP or EGFP plasmids with 1.6 μL FectoPRO, with 3mM valproic acid and 0.4% glucose added to the culture after 24 h. After 48 h, transfectants were washed twice with PBS and suspended in Assay Medium (L15 medium with 1% BSA). Each sample (50 μL) contained 2×10^6 cells/ml, 1nM Alexa 647-12G10 Fab, and indicated concentrations of cylic-ACRGDGWCG (cRGD) or MUPA-LDVPAAK peptide (LDVP) in Assay Medium. The mixture was allowed to equilibrate at 22°C for 1 h before flow cytometry (BD FACSCanto II) without washing.

CHO αIIbβ3 stable cells ($8x10^5$ plated in 2 mL DMEM with 10% FBS per well in 6 well plates) were transfected after 16 h when cells reached 90% confluency as described.[47] Talin1 head-EGFP or Flag-EGFP plasmids were mixed with 4 μL JetPrime in 200 μL JetPrime buffer and after 10 min added to each well. After 48 h, transfectants were washed twice with PBS and suspended in Assay Medium. Each sample (50 μL) contained 2×10^6 cells/ml, 5 nM Alexa 647-MBC319.4 Fab, and the indicated concentration of eptifibatide in Assay Medium. The mixture was allowed to equilibrate at 22°C for 1 h before flow cytometry (BD FACSCanto II) without washing. Mean fluorescence intensity (MFI) of Alexa 647 on EGFP positive single cells at each titrator concentration was fitted to a dose-response curve with three parameters (background MFI, maximum MFI, and the EC_{50} value which represents the K_d for ligand binding).

PAC-1 stainings were done on CHO cells stably expressing integrin αIIbβ3,[47] as shown in Figure S6A. CHO αIIbβ3 cells were transiently transfected with mock (Flag-EGFP) or talin1 head-EGFP constructs. 48 h post transfection, cells were stained with PAC-1, on ice, at indicated concentrations, with no additive (experimental), in the presence of 50 μM eptifibatide (background condition to block specific PAC1 binding), or in the presence of 1 μM LIBS-6 IgG (to define "maximal activation"). After 1 h primary staining and three washes, APC-anti IgM secondary antibody staining (2 μg/mL) was on ice for 30 min. Data was collected on EGFP positive single cells. Activation index shown in Figure S6B was calculated from data in Figure S6A based on the equation defined in Kim et al., 2012.[47]

$$\text{Activation index} = \frac{MFI_{\text{no additive}} - MFI_{+50\ \mu M\ \text{eptifibatide}}}{MFI_{+1\ \mu M\ \text{LIBS6}} - MFI_{+50\ \mu M\ \text{eptifibatide}}}$$

Multiple PAC-1 concentrations were used because the concentrations of primary and secondary antibodies were not given in the paper.[47]

Molecular modeling

The bent-closed (PDB ID code 7nxd) and extended-open (7nwl) conformations of α5β1[49] were superimposed on their βI domains. Running orientation.py of Pymol, the angle_between_domains command was used to align the closed hybrid domain on the open hybrid domain, which revealed a rotation axis of 66°. The region of 7nxd from the hybrid domain to the β-tail domain was opened 1/3 by rotating 22° on this axis, which showed complete separation from the α-leg. The model was saved as thirdopena5b1. To model partial integrin extension, the α and β-subunits of α5β1 (7nxd) and αIIbβ3 (3fcs), which is more bent, were separately superimposed on thirdopena5b1 using their EGF1 domains and thigh domains, respectively. Then, the angle_between_domains command was used to separately align the α and β-subunit calf-1 and EGF2 domains, respectively. The rotation vectors were used as described above to separately extend the α and β-subunits of α5β1 at their knees on the same trajectory as found between αIIbβ3 and α5β1 to make a more extended α5β1, which was saved as intermed, which is shown as the transition-like state in Figure 7. Further extension at the knees of intermed followed by superpositions on 7nxd and 7nwl were used to make the models for extended-closed and extended-open α5β1.

QUANTIFICATION AND STATISTICAL ANALYSIS

All of the statistical analyses and how significance was defined are described in Figure legends. Equations and software used are described in the STAR Methods.

CellPress
OPEN ACCESS

Supplemental figures

A Preparing FRET-pair labeled α5β1 soluble ectodomain

1mL scale transfection of Expi293 cells in FreeStyle293 medium at 2.5 million/mL for optimizating vector ratios

0.8 μg total plasmid including:
- 0.10 μg plasmid coding for α5 ectodomain
- 0.12 ug plasmid coding for eRF1E55D
- 0.15 μg - 0.43 μg plasmid coding for pyrrolysine tRNA synthetase & tRNA
- 0.43 μg - 0.15 μg plasmid coding for β1 ectodomain with double amber mutations

↓

Culture in FreeStyle293 medium supplemented with 200μM TCO*-Lys, with enhancers added after 24hrs

↓

After 96 hrs, anti-His western blot with the culture supernatant to find the optimal ratio between the plasmid coding for pyrrolysine tRNA synthetase & tRNA and the plasmid coding for β1 ectodomain with double amber mutations

↓

1L scale transfection to Expi293F cells with 800 μg total plasmids with optimized vector ratios, 1.0: 1.2: 2.3: 3.5, for α5 ectodomain, eRF1E55D, pyrrolysine tRNA synthetase & tRNA , and β1 ectodomain with double amber mutations

↓

After 96hrs, purification from culture supernatant with Ni-NTA affinity column

↓

Cleavage of C terminal purification tags with 0.1 mg/mL HRV3C protease and 1 mg/mL α5β1 ectodomain in Integrin Buffer for 48 hrs at 4°C

↓

Purification with Superdex 200 column in Integrin Buffer

↓

Labeling of purified integrin (1 mg/mL) with Sulfo-Cy3 tetrazine and Sulfo-Cy5 tetrazine (each at 10 μM) in Integrin Buffer for 1 hr at 22°C, followed by biotinylation with purified biotin ligase BirA (0.1 mg/mL) in Integrin Buffer for 18 hrs at 4°C

↓

Purification with Superdex 200 column in Integrin Buffer

↓

Flash freeze with liquid nitrogen and store in -80 °C

B Single mutants screened in α5β1 ectodomain

Mutation site on β1 (domain)	Expression relative to WT
Q1 (PSI)	~10%
R6 (PSI)	~5%
K9 (PSI)	~10%
S14 (PSI)	~30%
Q20 (PSI)	~20%
K51 (PSI)	~20%
Q280 (bI)	~30%
Y293 (bI)	~15%
K382 (Hybrid)	~30%
N383 (Hybrid)	~20%
N391 (Hybrid)	~20%
K417 (Hybrid)	~5%
K418 (Hybrid)	~30%
D522 (I-EGF2)	10%
N523 (I-EGF2)	0
N525 (I-EGF2)	~30%
E526 (I-EGF2)	~20%
N551 (I-EGF3)	~10%
K555 (I-EGF3)	~10%
N562 (I-EGF3)	~20%
P563 (I-EGF3)	~10%
S568 (I-EGF3)	~10%
S582 (I-EGF4)	~10%
R590 (I-EGF4)	~20%
K599 (I-EGF4)	~20%
Q643 (β-tail)	~20%

C Double mutants screened in α5β1 ectodomain for reporting integrin extension

Fluorophore labeling sites in β1	Measured higher FRET	Measured lower FRET
Q280 (βI) & N525 (IEGF2)	0.3~0.4	0.1~0.2
Q280 (βI) & K555 (IEGF3)	Most only show a low FRET state	
K418 (Hybrid) & K555 (IEGF3)	Most show the 0.5~0.6 FRET	
K418 (Hybrid) & S583 (IEGF4)	Most only show a low FRET state	
N391 (Hybrid) & N551 (IEGF3)	Most only show a low FRET state	
K418 (Hybrid) & N551 (IEGF3)	Most only show a low FRET state	
S14 (PSI) &R590 (IEGF4)	Most only show a low FRET state	
S14 (PSI) & K599 (IEGF4)	Most only show a low FRET state	
K51 (PSI) & Q643 (IEGF4)	Most only show a low FRET state	
K418 (Hybrid) & N562 (IEGF3)	Most show the 0.5~0.6 FRET	
K418 (Hybrid) & S568 (IEGF3)	Most show the 0.5~0.6 FRET	
K418 (Hybrid) & N525 (IEGF2)	Most show the 0.5~0.6 FRET	
N391 (Hybrid) & N562 (IEGF3)	0.5~0.6	0.3~0.4

D MW

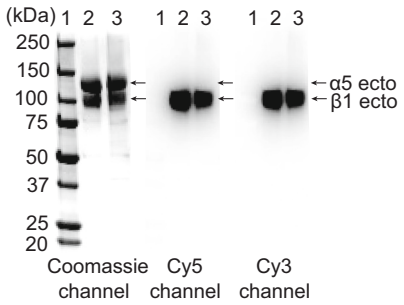

1. 15 uL Protein Standards
2. Closed↔Open ectodomain
3. Bent↔Extended ectodomain

Figure S1. Integrin α5β1 soluble ectodomain preparations used in the study, related to Figures 2 and 3

(A) Workflow for preparing FRET-pair labeled integrin α5β1 ectodomain. Integrin Buffer: 20mM HEPES, pH7.4, 150mM NaCl, 1mM Ca^{2+} and 1mM Mg^{2+}.

(B) Expression of single amber mutants tested by western blots against the His tag on the β1 ectodomain C terminus.

(C) Double amber mutants screened for reporting integrin extension; only a single pair was tested for reporting opening.

(D) SDS-PAGE (4–15%, non-reducing) of labeled α5β1 ectodomain (5 μg per lane) using the iBright imager Cy5 and Cy3 channels before Coomassie blue staining and the Coomassie blue channel after staining. Protein Standard is Precision Plus Protein All Blue Standards (BioRad).

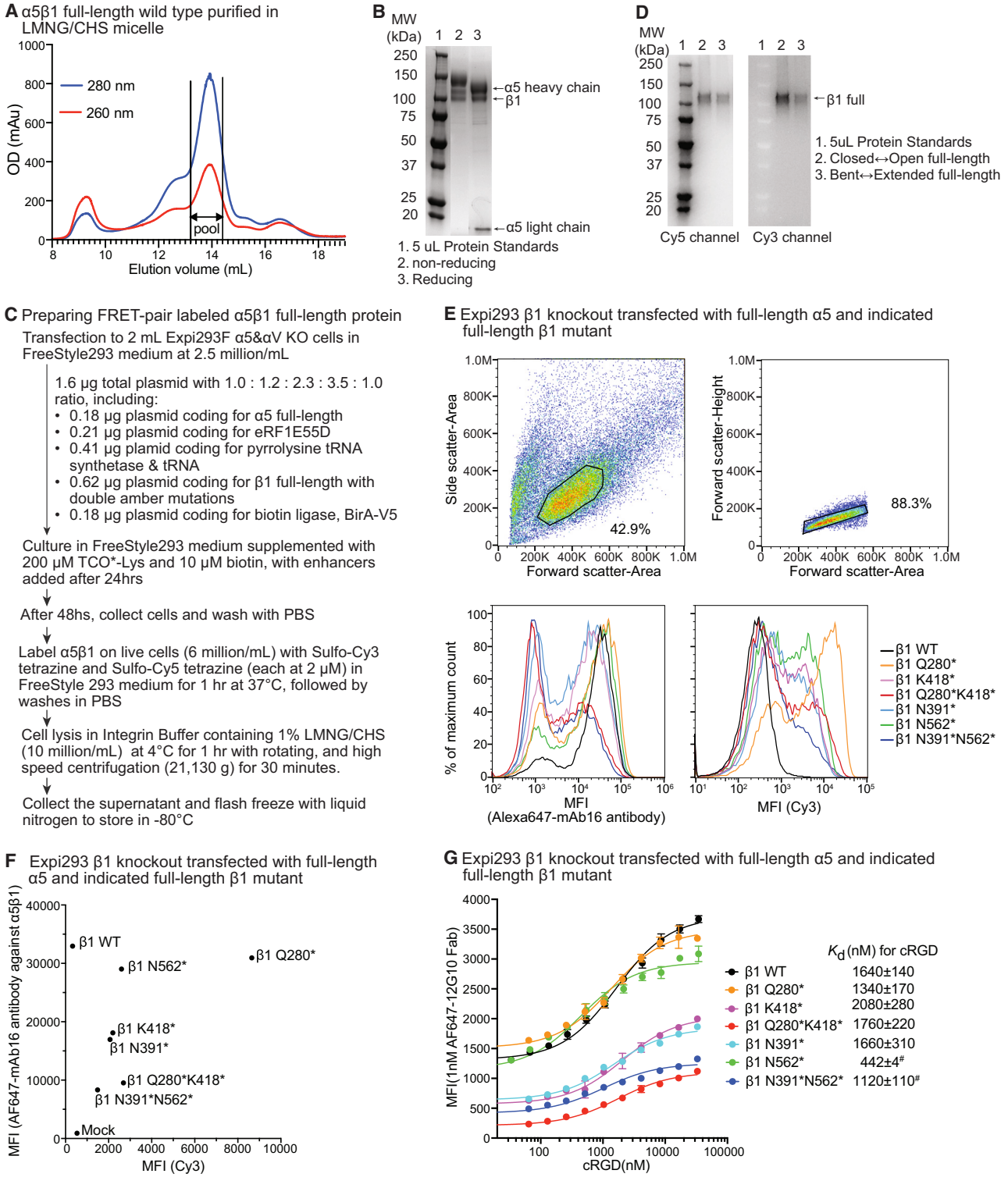

Figure S2. Integrin α5β1 full-length preparations used in the study, related to Figures 1, 4, 5, and 6

(A) Size exclusion chromatography profile of wild type α5β1 full-length protein purified in the presence of 0.01% (w/v) LMNG/CHS (10:1).

(B) Coomassie-stained SDS-page (4–20% gel) of purified wild type α5β1 full-length protein.

(C) Workflow for preparing FRET-pair labeled α5β1 full-length protein. Integrin Buffer: 20mM HEPES, pH7.4, 150mM NaCl, 1mM Ca^{2+} and 1mM Mg^{2+}.

(legend continued on next page)

(D) SDS-page (4–15%, non-reducing gel) of labeled α5β1 full-length protein after pulling down by Streptavidin Sepharose beads and imaging in the iBright Cy5 and Cy3 channels.

(E) Expression and Sulfo-Cy3 tetrazine labeling of α5β1 with amber mutations on the Expi293 β1 knockout transient transfectants. Transfection and labeling conditions are as described in Methods. Cells were washed after Sulfo-Cy3 labeling and further stained with 10nM Alexa 647-mAb16 (anti-α5β1) and subjected to flow cytometery to check α5β1 expression level and Cy3 labeling level.

(F) Expression vs. labeling level of indicated α5β1 mutants. Data is from Panel E.

(G) Affinity of Cy3 labeled α5β1 amber mutants for cRGD on transfected Expi293 β1 knockout cells. The binding of AF647-12G10 Fab (1nM) was measured as a function of cRGD concentration. Mean fluorescence intensity (MFI) was fitted to a dose-response curve with three parameters: background MFI, maximum MFI, and the EC_{50}. EC_{50} value is identical to K_d value of cRGD for α5β1. Errors in K_d values are SE from nonlinear least square fits, except for the value with "#" is difference from the mean from two experiments on different days. Protein Standard (in Panels B and D) is Precision Plus Protein All Blue Standards (BioRad). *: TCO*-Lys is incorporated at indicated position and labeled with Cy3.

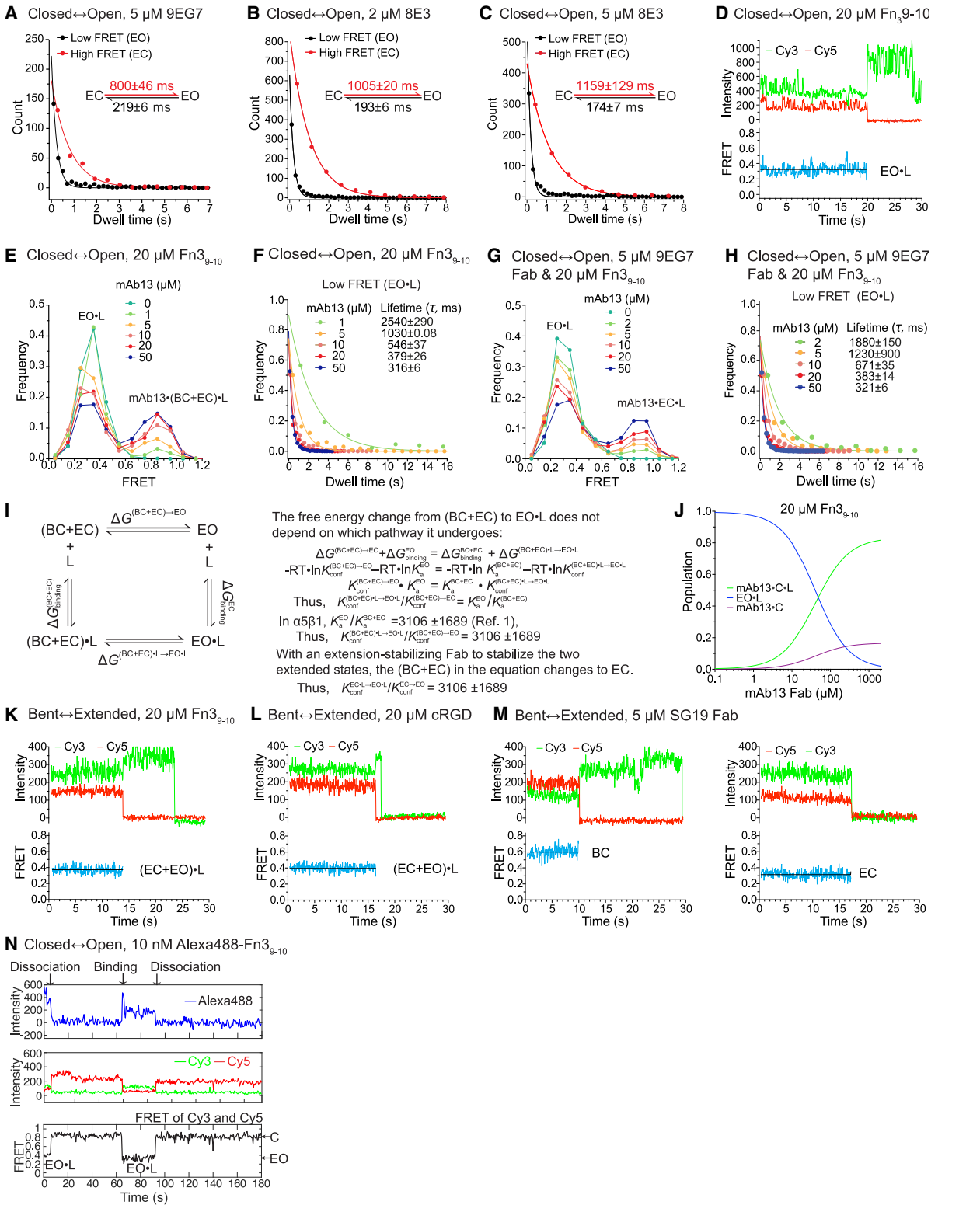

Figure S3. Measurements of conformational transition rates in the α5β1 ectodomain reporters, related to Figures 2 and 3

(A–I) Closed↔Open ectodomain reporter.

(A–C) Conformational transition rates with extension-stabilizing Fabs. Dwell time distributions of the low and high FRET states with single-exponential fits with indicated Fabs.

(legend continued on next page)

(D) Representative FRET time trace in the presence of saturating 20 μM $Fn3_{9-10}$ shows only the low FRET EO•L state.
(E–H) Conformational transitions in the presence of ligand in the absence and presence of extension-stabilizing Fab. The schemes of Figure 2G (in the absence of extension-stabilizing Fab) and Figure 2J (in the presence of extension-stabilizing Fab) were used to measure EO•L lifetime by temporarily stabilizing closed states with varying concentrations of mAb13 Fab. FRET efficiency histograms (E and G) and dwell time distributions of the low FRET state with single exponential decay fits (F and H) are shown.
(I) The thermodynamic cycle was used to calculate conformational equilibria that are used in main figures to calculate kinetic constants from the measured kinetic constants in the opposite direction. The ratio of the intrinsic binding affinities of the EO state and the closed states, 3106 ± 1689, is the average and sd of affinities measured from eight soluble α5β1 preparations[3] including the affinities of cRGD peptide for six ectodomain preparations, either clasped or unclasped with three different N-glycosylation forms (Figure 5 in Li et al.[3]), the affinities of cRGD peptide for high-mannose headpiece and semi-truncated ectodomain (Figure 6C in Li et al.[3]), and the affinity of $Fn3_{9-10}$ for the unclasped ectodomain with high mannose N-glycans (Figure 4D in Li et al.[3]). This average ratio of the intrinsic affinities was used for both the soluble α5β1 ectodomain in Figures 2I and 2K and full-length α5β1 in Figure 5G.
(J) Lack of transition between the BC•L and EC•L states cannot be experimentally demonstrated because at saturating $Fn3_{9-10}$, even at 70% w/v mAb13 (1 mM), EO•L would still be present. The data is calculated based on the affinity of $Fn3_{9-10}$ to EO state (Figure 1B), the ratio of the intrinsic binding affinities of the EO state and the closed states (Panel I), the equilibrium constant between the EO and the closed states calculated from the conformation transition rates between them (Figure 2D), and the affinity of mAb13 Fab to the closed states estimated based on data in panel E and G as 100 nM
(K–M) Representative FRET time traces of the ectodomain Bent↔Extended reporter when fully liganded (K and L) and when trapped in either the BC or EC states with closure-stabilizing Fab SG19 (M).
(N) Example time trace of Alexa 488-$Fn3_{9-10}$ (top panel) and FRET reporter (middle and bottom panels). Alexa 488, Cy3, and Cy5 were sequentially illuminated (200 ms/frame).

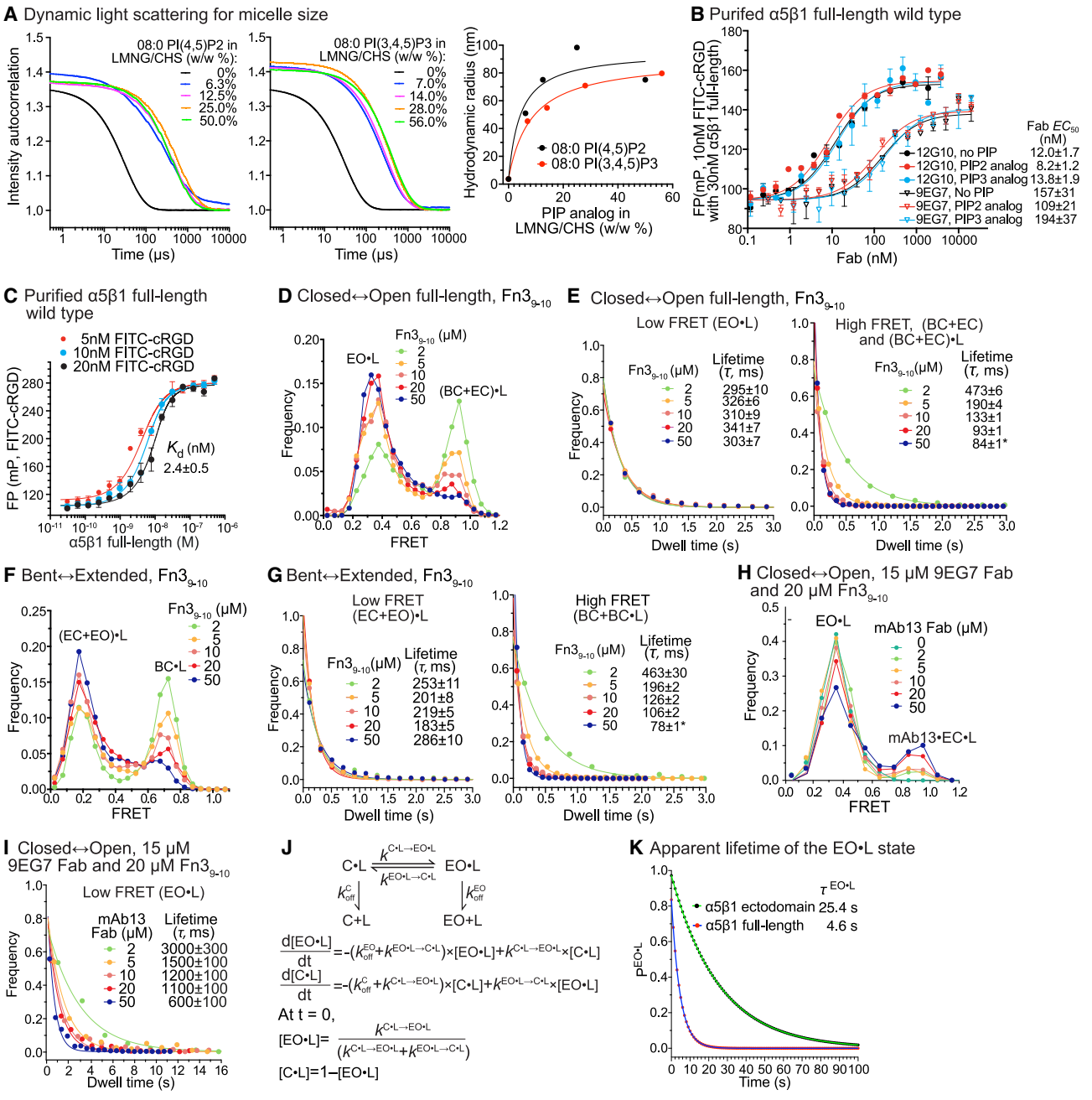

Figure S4. Measurements of conformational transition rates in full-length α5β1, related to Figures 4 and 5

(A) Influence of soluble PIP2 and PIP3 analogs on LMNG/CHS micelle size. Dynamic light scattering was performed on 0.1% LMNG/CHS with 08:0 PI(4,5)P2 (left) or 08:0 PI(3,4,5)P3 (middle) added as w/w % of LMNG/CHS. The hydrodynamic radius of the LMNG/CHS micelle was 3.4 nm, which was greatly increased by PIP2 or PIP3 analogs to ~80 nm (right).

(B) Addition of 20% PIP2 or PIP3 analog (w/w % of LMNG/CHS) with the attendant large increase in micelle size had little influence on the α5β1 full-length conformational equilibrium, as evidenced by the similar EC_{50} values of 12G10 and 9EG7 Fabs to stabilize the EO and EC+EO states, respectively. FP assays were with wild type α5β1 full-length (30 nM) binding to FITC-cRGD (10 nM) in 20 mM HEPES, pH 7.4, 150 mM NaCl, 1 mM Mg^{2+}, 1 mM Ca^{2+}, 0.01% LMNG/CHS. Values to the right of each plot are from nonlinear least square fits to dose-response curve and errors are SE from the fits.

(C) Related to Figure 4A, affinities of α5β1 wildtype full-length protein were measured using fluorescence polarization (FP) assays with indicated concentration of FITC-cRGD at 2 μM 12G10 Fab. Data were fit globally to different probe concentrations to account for the effect of high-affinity binding on ligand depletion. D, E, Closed↔Open full-length reporter in the presence of $Fn3_{9-10}$. F, G, Bent↔Extended full-length reporter in the presence of $Fn3_{9-10}$.

(D and F) FRET efficiency histograms.

(E and G) Dwell time distributions of the low and high FRET states with single-exponential fits. *In the presence of 50 μM $Fn3_{9-10}$, the lifetime of the high FRET states in both reporters became too short to accurately quantify (right panels). Hence, 50 μM $Fn3_{9-10}$ data were omitted in the fits in main text Figure 5F. H-I,

(legend continued on next page)

Measuring the dwell time of the EO•L state in the presence of saturating extension-stabilizing Fab 9EG7 and $Fn3_{9-10}$ in indicated concentrations of closure-stabilizing Fab mAb13.

(H) FRET efficiency histograms.

(I) Dwell time distributions of the low FRET state with single-exponential fit under indicated mAb13 concentration.

(J) Reaction scheme and equations for integrin ligand dissociation coupled with conformational changes; C=BC+EC.

(K) Simulated data (black and red dots) from the model shown in Panel J. Conformational transition rates between the C•L and EO•L states were measured in Figures 2I, 5E, and 5F for the ectodomain and full-length protein, respectively; and the intrinsic off-rates of the C and EO state were 1.4/s and $8.2*10^{-5}$/s (Figure 1B). Simulated data were fitted with single exponential decay curves (green and blue lines) to obtain lifetimes.

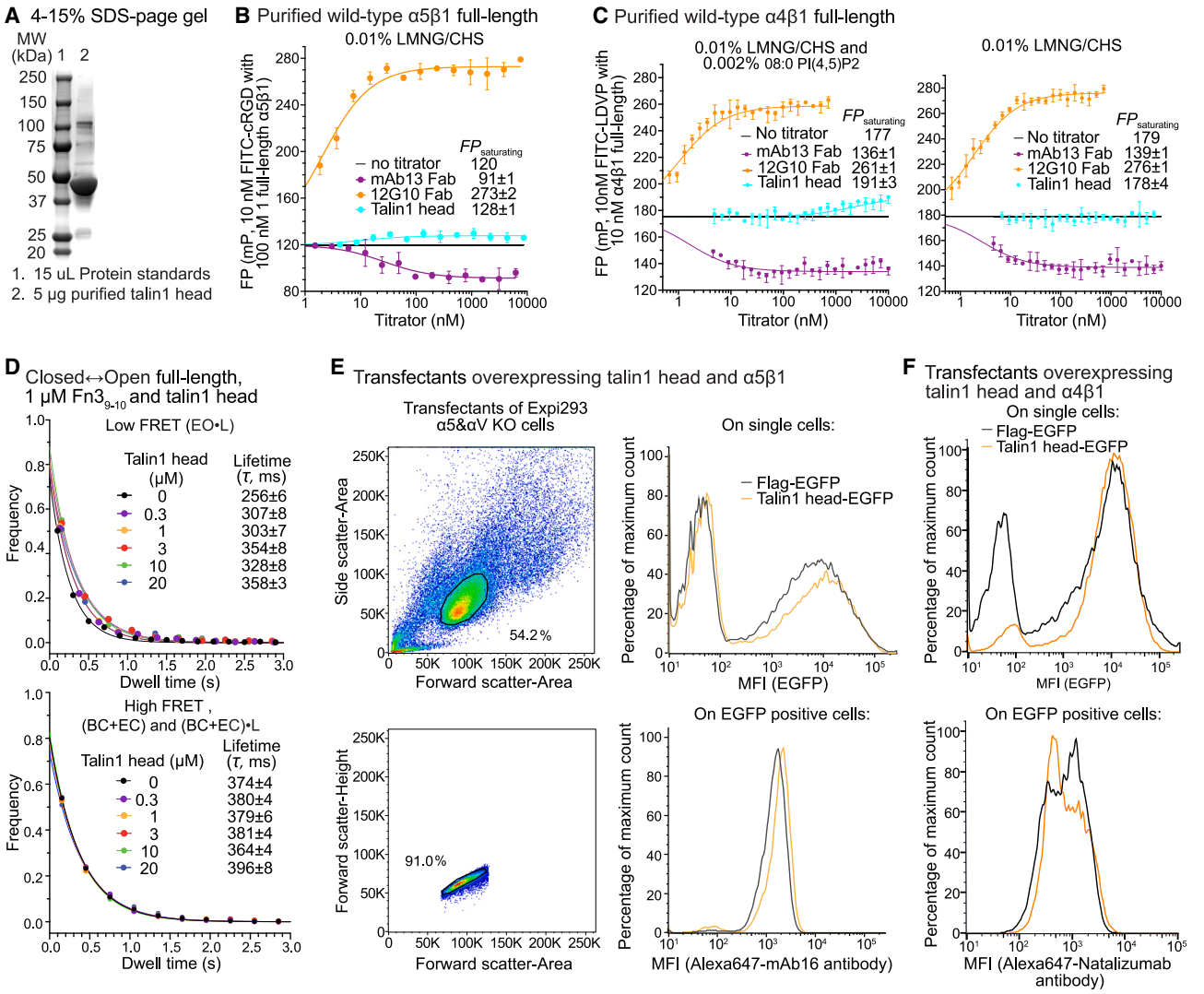

Figure S5. Measurements on the effects of the talin1 head on integrin activation, related to Figure 6

(A) Coomassie-stained, non-reducing SDS-PAGE of purified talin1 head.

(B) Dependence of α5β1 full-length (100 nM) binding to FITC-cRGD (10 nM) in FP assays on Fab or talin1 head concentration in 20 mM HEPES, pH7.4, 150 mM NaCl, 1 mM Mg^{2+}, 1 mM Ca^{2+} and 0.01% LMNG/CHS. Data were fitted to dose-response curves and errors are SE from the fits.

(C) Dependence of α4β1 full-length (10 nM) binding to FITC-LDVP (10 nM) in FP assays on Fab or talin1 head concentration in 20 mM HEPES, pH7.4, 150 mM NaCl, 1 mM Mg^{2+}, 1 mM Ca^{2+} and 0.01% LMNG/CHS with 0.002% 08:0 PI(4,5)P2 (left panel) or without (right panel). Data were fitted to dose-response curves and errors are SE from the fits.

(D) Dwell time distributions of the indicated FRET states with single-exponential fits under indicated conditions measured in 20 mM HEPES, pH7.4, 50 mM KCl, 0.1 mM Ca^{2+}, 1 mM Mg^{2+}, 0.01% LMNG/CHS, and 0.002% 08:0 PI(4,5)P2.

(E) Co-expression of talin1 head-EGFP fusion and integrin α5β1 on Expi293 α5&αV KO transient transfectants. Expi293 α5&αV KO cells were co-transfected with full-length α5 with talin1 head-EGFP fusion or Flag-EGFP. Talin1 head expression was checked by EGFP expression, and expression of α5β1 on EGFP-positive cells was checked with Alexa 647 labeled mAb16 antibody.

(F) Co-expression of talin1 head-EGFP fusion and integrin α4β1 on Expi293 α5&αV KO transient transfectants. Expi293 α5&αV KO cells were co-transfected with full length α4 with talin1 head-EGFP fusion or Flag-EGFP. Talin1 head expression was checked by EGFP expression, and expression of α4β1 on EGFP-positive cells was checked with Alexa 647 labeled natalizumab antibody.

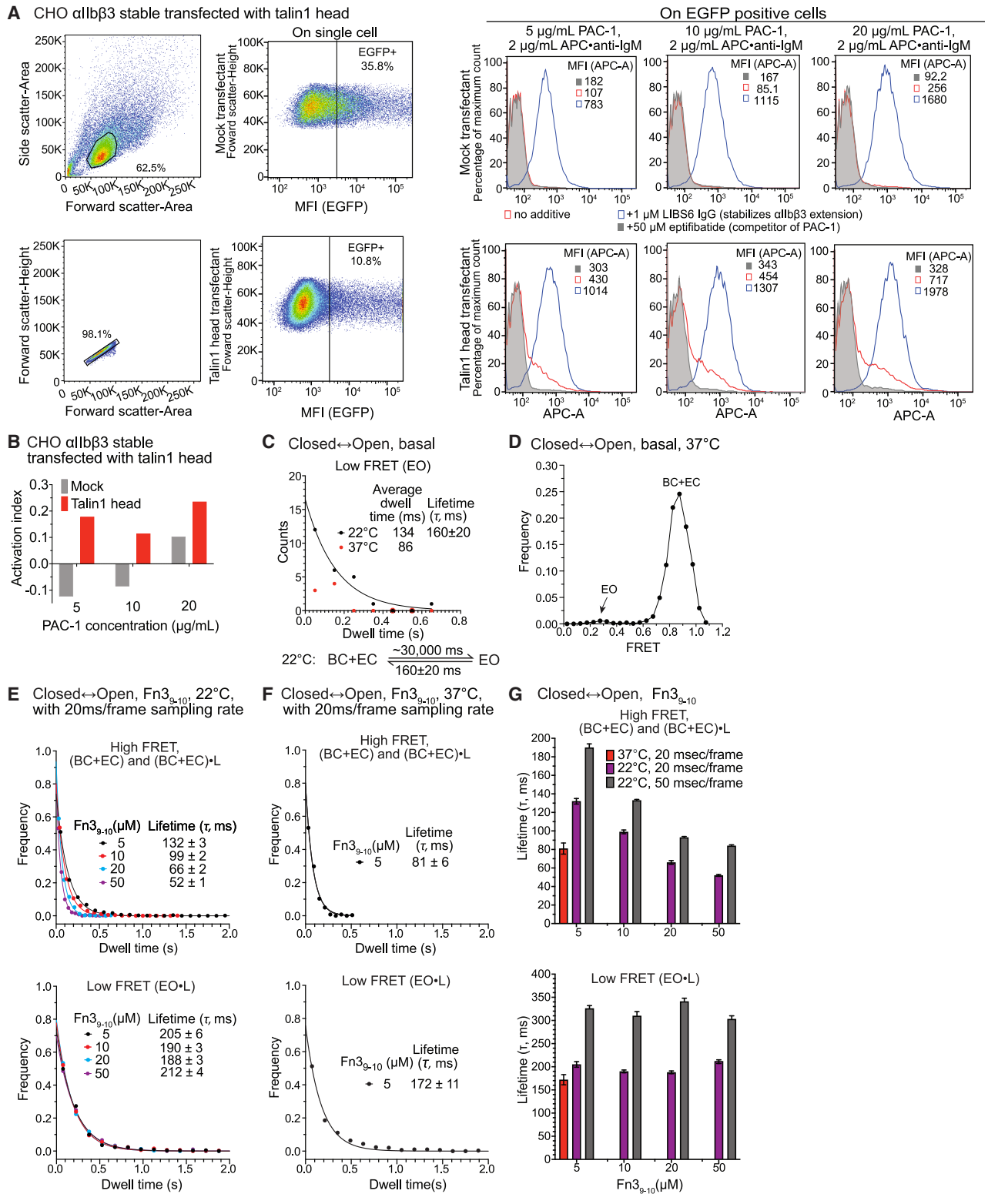

Figure S6. related to Figures 4, 5, and 6

(A) PAC-1 staining of CHO cells stably expressing integrin αIIbβ3.[47] CHO αIIbβ3 cells were transiently transfected with mock (Flag-EGFP) or talin1 head-EGFP constructs. 48 h post transfection, cells were stained with PAC-1, on ice, at indicated concentrations, with no additive (experimental), in the presence of 50 μM

(legend continued on next page)

eptifibatide (background condition to block specific PAC1 binding), or in the presence of 1 μM LIBS-6 IgG (to define "maximal activation"). After 1 h primary staining and three washes, APC-anti IgM secondary antibody staining (2 μg/mL) was on ice for 30 min. Data was collected on EGFP positive single cells.
(B) Activation index was calculated from data in panel A based on the equation defined in Kim et al., 2012.[47]

$$\text{Activation index} = \frac{MFI_{\text{no additive}} - MFI_{+50\ \mu M\ \text{eptifibatide}}}{MFI_{+1\ \mu M\ \text{LIBS6}} - MFI_{+50\ \mu M\ \text{eptifibatide}}}$$

Multiple PAC-1 concentrations were used because the concentrations of primary and secondary antibodies were not given in the paper.[47]
(C) Although transition to the open state in the absence of ligand was rare, we collected the dwell times of the few events that were observed. Fitting the dwell time distribution of the low FRET state was only possible at 22°C, yielding an estimate of the lifetime of the EO state. The lifetime of the combined BC+EC states was calculated from the lifetime of the EO state and the equilibrium constant $K_{conf}^{(BC+EC)\rightarrow EO} = 0.005$ from the population of the EO state of 0.5% (Figure 1C). This lifetime of ~30 s for the BC+EC states is compatible with the lack of FRET time traces showing more than one transition to the EO state and the length of traces prior to photobleaching (Figure 4D).
(D) FRET efficiency histogram under basal conditions at 37°C shows a higher population of the EO state than at 22°C (Figure 4B).
(E and F) Dwell time distributions of the high and low FRET states in varying concentrations of $Fn3_{9-10}$ with single-exponential fits with 20 ms/frame sampling rates at 22°C (E) and 37°C (F). Data collected at 37°C with $[Fn3_{9-10}] > 5$ μM could not be well fit to single-exponential distribution.
(G) Bar graphs comparing data collected in panels E and F to other measurements in this study, which used a 50 ms/frame sampling rate at 22°C. The comparisons suggest that short lifetimes (<300 ms) measured in the main figures may overestimate lifetimes at 37°C by ~2-fold.